Clinical, Cosmetic and Investigational Dermatology

Dovepress
Taylor & Francis Group

Open Access Full Text Article

ORIGINAL RESEARCH

Unraveling the Mechanism of Cuochuangling Pills in Rosacea Treatment: An Integrated Approach Combining Network Pharmacology, Bioinformatics, and Experimental Validation

Xiaoying Shen[1,2,*], Donghu Liu[2,3,*], Zhengjin Zhu[1,2], Shengjie Zhao[1,2], Xiaoning Yan[1,2], Meihong Li[1,2]

[1]Department of Dermatology, Shaanxi Provincial Hospital of Chinese Medicine, Xi'an, Shaanxi, People's Republic of China; [2]First Clinical Medical College, Shaanxi University of Chinese Medicine, Xianyang, Shaanxi, People's Republic of China; [3]Department of Traditional Chinese Medicine, Tangdu Hospital, Fourth Military Medical University, Xi'an, Shaanxi, People's Republic of China

*These authors contributed equally to this work

Correspondence: Meihong Li, Department of Dermatology, Shaanxi Provincial Hospital of Chinese Medicine, Xianyang, Shaanxi, People's Republic of China, Email 18799078@qq.com

Objective: This study aimed to systematically elucidate, for the first time, the therapeutic mechanism of Cuochuangling pills, (CCLP), a clinical herbal formulation for rosacea, through an innovative integrated approach combining network pharmacology, multi-method bioinformatics, and experimental validation.

Methods: Active components of CCLP were identified from the TCMSP database. Core therapeutic targets were screened by combining rosacea transcriptome data from GEO with differential expression analysis, weighted gene co-expression network analysis (WGCNA), and three machine learning algorithms. Molecular docking and dynamics simulations were employed to evaluate ligand-receptor binding stability. An LL-37-induced murine rosacea model was established and treated with low-, medium-, and high-dose CCLP for 7 days. Erythema area and severity scores were recorded. Histopathological examination and mast cell infiltration were assessed via H&E and toluidine blue staining, respectively. Inflammatory cytokines (IL-1β, IL-6, TNF-α) were measured by ELISA, and protein expression of TLR2, KLK5, and MMP9 was analyzed by immunohistochemistry.

Results: IL-1β was identified as the core target, with KEGG enrichment analysis highlighting inflammatory pathways including NF-κB. Molecular docking revealed a strong binding affinity between quercetin and IL-1β (−7.4 kcal/mol), further confirmed by stable binding in molecular dynamics simulations. In vivo, medium and high doses of CCLP significantly reduced erythema, severity scores, and mast cell infiltration, while downregulating IL-1β, IL-6, TNF-α, TLR2, KLK5, and MMP9 expression.

Conclusion: CCLP alleviates LL-37-induced rosacea-like dermatitis by modulating the TLR2/NF-κB signaling pathway, leading to reduced inflammatory response and mast cell infiltration.

Keywords: rosacea, traditional Chinese medicine, network pharmacology, bioinformatics, molecular docking, molecular dynamics simulations

Introduction

Rosacea is a chronic inflammatory dermatosis characterized by a central facial distribution of clinical features including transient flushing, persistent erythema, telangiectasia, papules, and pustules. In severe cases, phymatous changes such as rhinophyma may develop. Patients frequently report accompanying cutaneous symptoms including dryness, pruritus, burning, or stinging sensations.[1] The condition demonstrates a predilection for young and middle-aged adults, with a notably higher prevalence among females.[2] Clinically, rosacea is classified into four principal subtypes: erythemato-telangiectatic (ETR), papulopustular (PPR), phymatous (PHR), and ocular rosacea (OR).[3] Epidemiological studies indicate that the condition affects approximately 5.5% of the global population, with recent data suggesting a steadily

https://doi.org/10.2147/CCID.S579507
Received: 6 November 2025
Accepted: 17 February 2026
Published: 4 March 2026

increasing incidence worldwide.[4,5] The visible nature of facial lesions, combined with the chronic, relapsing course of the disease, frequently contributes to profound psychosocial sequelae such as diminished self-esteem, anxiety, and depression, substantially impairing patients' quality of life and psychological well-being.

The pathogenesis of rosacea is multifactorial, involving genetic predisposition, innate and adaptive immune dysregulation, neurovascular dysfunction, and alterations in the skin microbiome. Recent genetic studies have identified several susceptibility genes, including human leukocyte antigen (HLA), Toll-like receptor 2 (TLR2), interleukin-17 (IL-17), and the cathelicidin antimicrobial peptide (CAMP) gene.[2] Consistent with these findings, elevated expression of TLR2 and its downstream effector LL-37 in lesional skin underscores the critical role of innate immune activation in disease initiation and progression. A key pathological feature is the infiltration of mast cells into inflammatory sites and the nuclear factor-kappa B (NF-κB)-mediated release of pro-inflammatory mediators, such as IL-1β, IL-6, IL-17, interferon-gamma (IFN-γ), matrix metalloproteinases (MMP2, MMP9), and tumor necrosis factor-alpha (TNF-α). The recruitment of $CD4^+$ T-cells further amplifies the inflammatory cascade,[6] leading to the characteristic clinical manifestations. Current treatment modalities for rosacea include topical agents (eg, oxymetazoline, brimonidine, azelaic acid),[7,8] systemic therapies (eg, isotretinoin, doxycycline),[9] and energy-based devices such as pulsed dye laser (PDL) and intense pulsed light (IPL).[10] However, due to an incomplete understanding of the disease etiology, these interventions are often associated with significant limitations, including undesirable side effects, prolonged treatment courses, and high rates of relapse upon cessation. Long-term use of oral antibiotics raises concerns regarding microbial dysbiosis and potential impacts on hepatic, renal, and metabolic function. Similarly, phototherapeutic options are limited in their applicability and often fail to provide sustained control of symptoms or prevent disease recurrence in a substantial proportion of patients.

Given the limitations of current therapies, complementary approaches such as traditional Chinese medicine (TCM) have gained attention. CCLP is a modern pill formulation derived from the classical traditional Chinese medicine prescription Xianfang HuoMingYin. It is an institutional preparation developed and approved (Shaanxi Pharmaceutical Preparation Approval No. Z20210084000) by the Shaanxi Provincial Hospital of Traditional Chinese Medicine. The formula comprises multiple herbal components, including Leonuri Herba, Mori Cortex, Hedyotis Diffusae, Scutellariae Radix, Rhei Radix et Rhizoma, Rehmanniae Radix, Paeoniae Radix Rubra, Moutan Cortex, Angelicae Sinensis Radix, Carthami Flos, Forsythiae Fructus, Platycodi Radix, Angelicae Dahuricae Radix, and Glycyrrhizae Radix et Rhizoma. Emerging pharmacological evidence suggests that the base prescription, Xianfang Huoming Yin, exerts anti-inflammatory effects by suppressing the activation of the NF-κB signaling pathway, thereby inhibiting the production of pro-inflammatory cytokines.[11] Key individual constituents contribute to this overall activity through diverse mechanisms. Hedyotis Diffusae is rich in polysaccharides known for their broad pharmacological properties, including anti-inflammatory, antioxidant, and immunomodulatory activities.[12] Licorice (Glycyrrhizae Radix et Rhizoma), containing glycyrrhizic acid as a major bioactive compound, modulates inflammatory responses via the NF-κB and MAPK pathways and inhibits reactive oxygen species (ROS) and pro-inflammatory cytokines such as TNF-α, IL-6, and IL-1β.[13] Similarly, Moutan Cortex (Moutan Cortex) and its active components (eg, paeonol and paeoniflorin) demonstrate significant anti-inflammatory and anti-allergic effects, with its ethanol extract shown to reduce mast cell counts and suppress the release of TNF-α and IL-6.[14] The therapeutic efficacy of CCLP in rosacea is likely attributable to the synergistic interactions among these constituents. However, current observations on the efficacy of traditional Chinese medicine (TCM) in rosacea primarily originate from clinical practice, lacking a systematic framework that integrates multi-omics prediction with experimental validation to decipher the mechanism of action of specific herbal formulas. Although the anti-inflammatory properties of the individual herbs contained in CCLP are well-recognized, the precise molecular targets and pathways through which CCLP exerts its therapeutic effects against rosacea remain unclear. This knowledge gap limits both the scientific understanding and the potential for optimization of TCM-based rosacea treatments.

Furthermore, bioinformatic algorithms, such as differential gene expression analysis, weighted gene co-expression network analysis (WGCNA), and machine learning, have been widely employed to predict disease biomarkers and therapeutic targets. Among these, WGCNA identifies highly correlated gene modules and reveals relationships between modules as well as between modules and external sample traits, thereby facilitating the prediction of disease signatures and therapeutic targets. Machine learning algorithms excel at capturing non-linear relationships and identifying subtle patterns that may be missed by conventional methods, thus promoting accurate feature selection.[15] In particular, the integrated application of the least

absolute shrinkage and selection operator (LASSO), support vector machine recursive feature elimination (SVM-RFE), and random forest (RF) has demonstrated superior performance in developing predictive models for target identification, significantly improving both the accuracy and reliability of candidate biomarker selection.

Network pharmacology facilitates the modernization of TCM by constructing "herb-target-pathway" networks, which provide a visual representation of the complex interactions among bioactive compounds, genes, and diseases. In the present study, we initially employed a network pharmacology-based approach to screen potential therapeutic targets of CCLP against rosacea. Subsequently, we performed differential expression analysis and weighted gene co-expression network analysis (WGCNA) on public transcriptomic datasets, followed by an in-depth screening and confirmation of key targets using three machine learning algorithms. Insights derived from these complementary analytical strategies suggest a coherent pathogenic axis: TLR2 activation stimulates the expression of KLK5 and MMP9, leading to the generation of the antimicrobial peptide LL-37. LL-37, in turn, can further activate TLR2 and potently induce the expression of pro-inflammatory cytokines, most notably IL-1β. Acting as a pivotal upstream regulator, IL-1β drives the activation of the NF-κB signaling pathway, resulting in the sustained production of cytokines (eg, TNF-α, IL-6), chemokines, and matrix-degrading enzymes. This cascade ultimately exacerbates inflammatory responses, angiogenesis, and tissue remodeling, underscoring the therapeutic significance of targeting IL-1β. To validate this prediction, we conducted molecular docking and molecular dynamics simulations to assess protein-ligand interactions, complemented by in vivo animal experiments to confirm the therapeutic efficacy of CCLP. Although this integrated workflow has inherent limitations, it not only proposes a novel mechanistic framework for TCM in the treatment of rosacea but also provides a valuable theoretical foundation for the development of herbal formulations and their future clinical application.

Materials and Methods

Prediction and Acquisition of CCLP Targets

Potential active ingredients of CCLP were retrieved from the TCMSP database (https://www.tcmsp-e.com/). These compounds were screened against established pharmacokinetic criteria: oral bioavailability (OB) ≥ 30% and drug-likeness (DL) ≥ 0.18. The canonical SMILES structures of the resulting compounds were acquired from PubChem (https://pubchem.ncbi.nlm.nih.gov). Corresponding protein targets were subsequently predicted using the SwissTargetPrediction platform (https://www.swisstargetprediction.ch).

Rosacea Target Acquisition and DEGs Screening

Rosacea-associated genes were compiled from multiple public databases, including GeneCards (https://www.genecards.org/; 520 genes), OMIM (https://omim.org/; 5 genes), and the Comparative Toxicogenomics Database (CTD; https://ctdbase.org/; 7691 genes). Transcriptomic data were obtained from the Gene Expression Omnibus (GEO) under accession numbers GSE65914 (comprising 20 healthy controls and 38 rosacea samples) and GSE303282 (3 healthy controls and 3 rosacea samples). Gene expression values were normalized using the $\log_2(x + 1)$ transformation. Differential expression analysis was conducted with the "limma" package in R, applying a significance threshold of $|\log_2 \text{fold change}| > 1$ and an adjusted p-value < 0.05. The top 30 differentially expressed genes were visualized in a volcano plot generated with the "ggplot2" package. Principal component analysis (PCA) was performed to evaluate sample distribution and dataset quality.

WGCNA Screening Module Objectives

Weighted gene co-expression network analysis was performed on the GSE65914 dataset using the Rstudio package "WGCNA"to identify gene modules associated with rosacea. Co-expression networks were constructed by selecting an appropriate soft-thresholding power to ensure scale-free topology. Resulting modules were correlated with clinical traits to identify rosacea-relevant gene clusters. Functional genes from these key modules were subsequently extracted for further analysis. Visualization outputs included sample dendrograms and trait heatmaps, module clustering dendrograms, scale-free topology and mean connectivity plots, module-trait relationship heatmaps, and representative module network diagrams. Finally, potential therapeutic targets were identified by intersecting the CCLP active ingredient targets with the

rosacea-associated genes obtained from WGCNA, and the results were visualized using the online Microbiome Bioinformatics Platform (https://www.bioinformatics.com.cn).

Construction of Protein-Protein Interaction Network and Enrichment Analysis

The screened gene targets were imported into the STRING database (https://cn.string-db.org/) to construct a protein-protein interaction (PPI) network. Use CytoScape 3.10.0 software to filter core targets and build a PPI network topology. The core targets were imported for enrichment analysis using the Microbiome online platform (http://www.bioinformatics.com.cn/) and the results were visualized.

R Algorithm to Screen Core Genes

The intersecting genes were analyzed by "R" using "e1071", "caret", "randomForest", "sigFeature", "tidyverse", "glmnet", "msvmRFE.R", "VennDiagram" packages for SVM algorithm model training and evaluation, and "randomForest" for Random Forest analysis. The "randomForest" package is used to train the random forest model, and the "limma" package is used to filter out the significant features, and the "ggpubr" package is used to visualize the results. In the LASSO regression analysis, "glmnet" is used to train the LASSO model, and "tidyverse" and "broom" packages are used to visualize and present the data. The intersection of the genes screened by the three algorithms was used to obtain the final core genes, and the results were visualized using the microbiome platform (http://www.bioinformatics.com.cn/).

ROC Diagnostic Model

The genes screened by PPI network mapping were intersected with the genes screened by R programming algorithm to obtain the final core genes. The time-dependent subject operating characteristic (ROC) curves were evaluated by R using "ggplot2", "enrichplot" and "pROC" packages. The ROC diagnostic models of the seven core genes in the training dataset GSE65914 and the validation dataset GSE303282 were plotted.

Analysis of the Relationship Between Core Genes and Immune Infiltration

In order to study the distribution of 22 types of immune cells in patients with rosacea and the relationship between core genes and immune cells, we visualized the results of the immune infiltration analysis of the "CIBERSORT" module through the microbiology platform.

Single-Gene GSEA Analysis

Gene Set Enrichment Analysis (GSEA) of IL1B was performed on dataset GSE65914 using the gene set file "c2.all.v2025.1.Hs.symbols.gmt"obtained from the MSigDB database. The analysis was implemented in R with the following packages: clusterProfiler for enrichment analysis, org.Hs.egdb for gene identifier conversion, enrichplot for visualization, and future/future.apply for parallel computing. The results were visualized to identify significantly enriched pathways associated with IL1B expression.

Molecular Docking

The SDF files of key active components were acquired from the PubChem database (https://pubchem.ncbi.nlm.nih.gov). Energy minimization was conducted using ChemBio3D, and the structures were converted to PDB format with PyMOL 2.1.0. The crystal structure of IL-1β (PDB ID: 1L2H) was retrieved from the RCSB PDB database (https://www.rcsb.org), followed by removal of water molecules and native ligands using PyMOL 2.1.0. The receptor protein was processed in AutoDock Tools 1.5.6 for hydrogen addition and charge assignment. Active ligands were prepared by adding hydrogens, defining rotatable bonds, and saving in PDBQT format. Molecular docking was performed using AutoDock Vina 2.0 in PyRx 0.8 to compute binding free energies. The resulting conformations were visualized with Discovery Studio 2019 to analyze interaction patterns between ligands and the target protein.

Molecular Dynamics Simulations

All-atom molecular dynamics (MD) simulations were performed using the Amber 2020 software package. The ff14SB force field was applied for proteins, while the GAFF force field was used to parameterize small-molecule ligands. Solvation was carried out with the TIP3P water model in an octahedral periodic boundary box, and charge neutrality was maintained by adding appropriate numbers of sodium and chloride ions. Prior to production simulation, the system underwent energy minimization involving 10,000 steps of steepest descent optimization with positional restraints applied to ligands. Following equilibration, a 100-ns unrestrained MD simulation was conducted under physiological conditions (300 K, 1 bar) using standard coupling algorithms. Trajectory coordinates and energies were recorded at 10-ps intervals for subsequent analysis.

Experiments

Animals

Female BALB/c mice (6–8 weeks old, 22 ± 2 g) were supplied by the Experimental Animal Center of Xi'an Jiaotong University School of Medicine [License No.: SCXK(Shaanxi) 2023–002; Animal Quality Certificate No.: 0012260]. The mice were housed under controlled conditions (20–22°C, 48% ± 5% humidity) with a 12-hour light/dark cycle and had ad libitum access to food and water. Following a one-week acclimation period, all experimental procedures were initiated. All animal experimental procedures were conducted in strict accordance with the 3Rs principles (Replacement, Reduction, and Refinement) and were approved by the Animal Ethics Committee of Shaanxi Provincial Hospital of Chinese Medicine (Approval No.: (2025) 15).

Drugs

CCLP was provided by Shaanxi Provincial Hospital of Traditional Chinese Medicine (Shaanxi Pharmaceutical Preparation Approval No. Z20210084000) and comprises 14 herbal components, as detailed in Table 1. Doxycycline hydrochloride tablets were obtained from Jiangsu Li anhuan Pharmaceutical Co., Ltd. (JLPC, National Drug Approval No. H32021266).

Table 1 CCLP Drug Ingredient List

Chinesename	Herb'sEnglishname	Herb'sLatinname
YMC	CommonMotherwortHerb	LeonuriHerba
SBP	WhiteMulberryRoot-Bark	MoriCortex
BHSSC	SpreadingHedyotisHerb	HerbaHedyotisDiffusae
HQ	BaikalSkullcapRoot	ScutellariaeRadix
DH	ChineseRhubarbRootandRhizome	RheiRadixetRhizoma
SDH	AdhesiveRehmanniaRootTuber	RehmanniaeRadix
CS	RedPaeoniaeTrichocarpae	PaeoniaeRadixRubra
MDP	TreePeonyRoot-bark	MoutanCortex
DG	ChineseAngelicaRoot	AngelicaeSinensisRadix
HH	SafflowerFlower	CarthamiFlos
LQ	ChineseGoldthread	ForsythiaeFructus
JG	PlatycodonRoot	PlatycodiRadix
BZ	ChineseAngelicaRoot	AngelicaeDahuricaeRadix
GC	LiquoriceRoot	GlycyrrhizaeRadixetRhizoma

Reagents

The following reagents were used in this study: antimicrobial peptide LL-37 (Taojin Bio, Cat# 154947–66-7 freebase); mouse IL-6 ELISA kit (Superior Bio, Cat# SYP-M0031); mouse IL-1β ELISA kit (Superior Bio, Cat# SYP-M0026); mouse TNF-α ELISA kit (Superior Bio, Cat# SYP-M0036); anti-KLK5 antibody (Naturebios, Cat# A70679); anti-MMP9 antibody (Naturebios, Cat# A86257); anti-TLR2 antibody (Naturebios, Cat# A45387); hematoxylin and eosin (H&E) staining kit (Sigma-Aldrich, Cat# H9627); and toluidine blue staining solution (Solarbio, Cat# G3670). All reagents were supplied by Shaanxi Dekun Biomedical Co., Ltd.

Model Preparation and Administration

Thirty mice were randomly assigned to six groups (n=5 per group): control group, model group, the doxycycline (DOX)-treated positive group, CCLP low-dose group, CCLP medium-dose group, and CCLP high-dose group. One day prior to modeling, the dorsal hair of all mice was shaved to create a 3×3 cm area. Except for the control group, all mice received subcutaneous injections of LL-37 (320 μmol/L, 40 μL per injection) at 0, 12, 24, and 36 hours. The control group received equal volumes of PBS instead. Twenty-four hours after the final modeling injection, drug administration began: the model group received 0.2 mL saline via gastric gavage daily; the CCLP groups received 26.5, 53, and 106 mg/kg of CCLP respectively; and the positive group received 30 mg/kg doxycycline hydrochloride solution. All treatments were administered once daily for 7 consecutive days.

Erythema Degree Score and Erythema Area Measurement

Six hours following the final administration, the injection site on the dorsal skin of each mouse was photographed. The severity of skin lesions was assessed based on erythema scores and affected area. The erythema scoring criteria were as follows: 0, no erythema; 1, barely visible erythema; 2, mild but distinct erythema with vague margins; 3, noticeable erythema with well-defined margins; 4, intense erythema with sharp margins. A 1 cm^2 circular reference card was placed adjacent to the injection site during imaging for scale calibration. The erythema area was quantified from the photographs using ImageJ software.After assessment, the mice were euthanized via intraperitoneal injection of 1% sodium pentobarbital (0.2 mL/10 g body weight). Dorsal skin lesion tissues were harvested and divided into two portions: one was fixed in 4% paraformaldehyde for subsequent Hematoxylin-eosin staining (H&E), toluidine blue staining, and immunohistochemical analysis; the other was snap-frozen and stored at –80°C for enzyme-linked immunosorbent assay (ELISA).

Dermatopathological and Morphological Changes at the Injection Site on the Back of Mice Detected by H&E Staining

Skin tissue samples fixed in 4% paraformaldehyde were processed through dehydration, paraffin embedding, and sectioning. The sections were stained with H&E for histopathological evaluation. Initial morphological assessment was performed under a light microscope at 200× magnification. For quantitative analysis, five random fields per sample were examined at 400× magnification, and the number of inflammatory cells in each field was counted. The average cell count across the five fields was calculated for each sample.

Toluidine Blue Staining to Detect the Number of Mast Cells

Paraffin-embedded tissue sections (5 μm thickness) were prepared and stained following the Toluidine Blue Staining Kit protocol. Mast cells were identified by their characteristic metachromatic purple-blue granules. For each sample, five randomly selected fields were examined under 400× magnification. The number of mast cells in each field was manually counted, and the average count across the five fields was calculated for statistical analysis.

Detection of IL-6, IL-1β and TNF-α Levels in Skin Lesion Tissues by ELISA

Frozen skin lesion tissues (30 mg samples) were homogenized in pre-cooled PBS using an ice bath. The homogenates were centrifuged at 4°C (10 cm radius, 4000 × g, 10 min) to collect the supernatant. Total protein concentration was determined using a BCA protein assay kit, and samples were normalized to equal concentrations prior to performing ELISA according to the manufacturer's instructions.

Immunohistochemical Staining for TLR2, KLK5, MMP9 Protein Expression

Paraffin-embedded tissue sections were deparaffinized, subjected to antigen retrieval, and blocked with serum. The sections were incubated overnight at 4°C with the following primary antibodies diluted at 1:100: anti-TLR2, anti-KLK5, and anti-MMP9. After washing with PBS (3 × 5 min), the sections were incubated with appropriate secondary antibodies at 37°C for 30 min. Following additional washes, immunoreactivity was visualized using DAB chromogenic development. The sections were then counterstained with hematoxylin, differentiated in hydrochloric acid alcohol, dehydrated, and mounted. For each sample, five random fields were examined at 200× magnification. Quantitative analysis of protein expression was performed using ImageJ software by measuring the mean optical density of positive staining.

Statistical Methods

Data are presented as the mean ± standard deviation. Statistical differences between groups were determined by one-way analysis of variance (ANOVA) followed by Tukey's post hoc test for multiple comparisons, using GraphPad Prism software (version 10.1.2). A P-value of less than 0.05 was considered statistically significant.

Results

Screening for CCLP and Rosacea Targets

Based on the screening criteria of drug-likeness (DL) ≥ 0.18 and oral bioavailability (OB) ≥ 30% in the TCMSP database, active components of CCLP were identified. Subsequent prediction using the SwissTargetPrediction database yielded 703 potential drug targets. Meanwhile, a total of 8042 rosacea-related targets were retrieved from the GeneCards, OMIM, and CTD databases. An active component–target network was constructed and visualized using Cytoscape 3.10.0 (Figure 1A). A Venn diagram was generated to illustrate the intersection between drug and disease targets (Figure 1B). Core targets derived from the intersection were further subjected to Gene Ontology (GO) biological function and Kyoto Encyclopedia of Genes and Genomes (KEGG) pathway enrichment analysis using the clusterProfiler package in R (Figure 1C and D).

Screening for Rosacea Targets

Analysis of the GSE65914 dataset from the GEO database identified 1096 differentially expressed genes (DEGs), comprising 407 upregulated and 689 downregulated genes. A volcano plot illustrates the distribution of these DEGs (Figure 2A), while a clustering heatmap displays the expression patterns of the significant DEGs, with red indicating upregulated genes, blue indicating downregulated genes, and gray representing non-significant genes (Figure 2B). Comparison of these DEGs with predicted CCLP targets through Venn analysis identified 10 upregulated (Figure 2C) and 36 downregulated genes (Figure 2D) as potential CCLP-responsive targets. Principal component analysis (PCA) revealed clear separation between sample groups with minimal overlap, indicating distinct transcriptional profiles and adequate sample representation for subsequent analyses (Figure 2E).

Screening of WGCNA Module Targets

To satisfy scale-free topology requirements for weighted gene co-expression network analysis (WGCNA), soft-thresholding power values were tested from 1 to 30. The corresponding scale-free fit indices and mean connectivity were calculated for each network (Figure 3A). A power value of 4 was selected as it achieved the optimal balance between scale-free topology fit and network connectivity. Using this parameter, a weighted co-expression network was constructed, classifying 25,849 genes into 13 distinct modules, as shown in the gene clustering dendrogram (Figure 3B). Module assignment and sample relationships are displayed in the sample clustering diagram, where the upper panel shows the gene dendrogram and the lower panel illustrates gene distribution across modules, with colors representing module membership and DynamicTreeCut indicating module identification (Figure 3C). A heatmap visualizes the clustering of all genes within the co-expression network (Figure 3D). Module-trait relationships were assessed using Pearson correlation analysis, revealing that the blue module showed the most significant association with rosacea (p-value < 0.001), containing 5454 genes (Figure 3E). Integration of CCLP targets, rosacea-related genes, GEO differentially expressed genes, and WGCNA-derived targets identified 17 overlapping genes (Figure 3F). Correlation scatter plots of the blue module confirmed that gene expression patterns were consistent with overall module trends (Figure 3G).

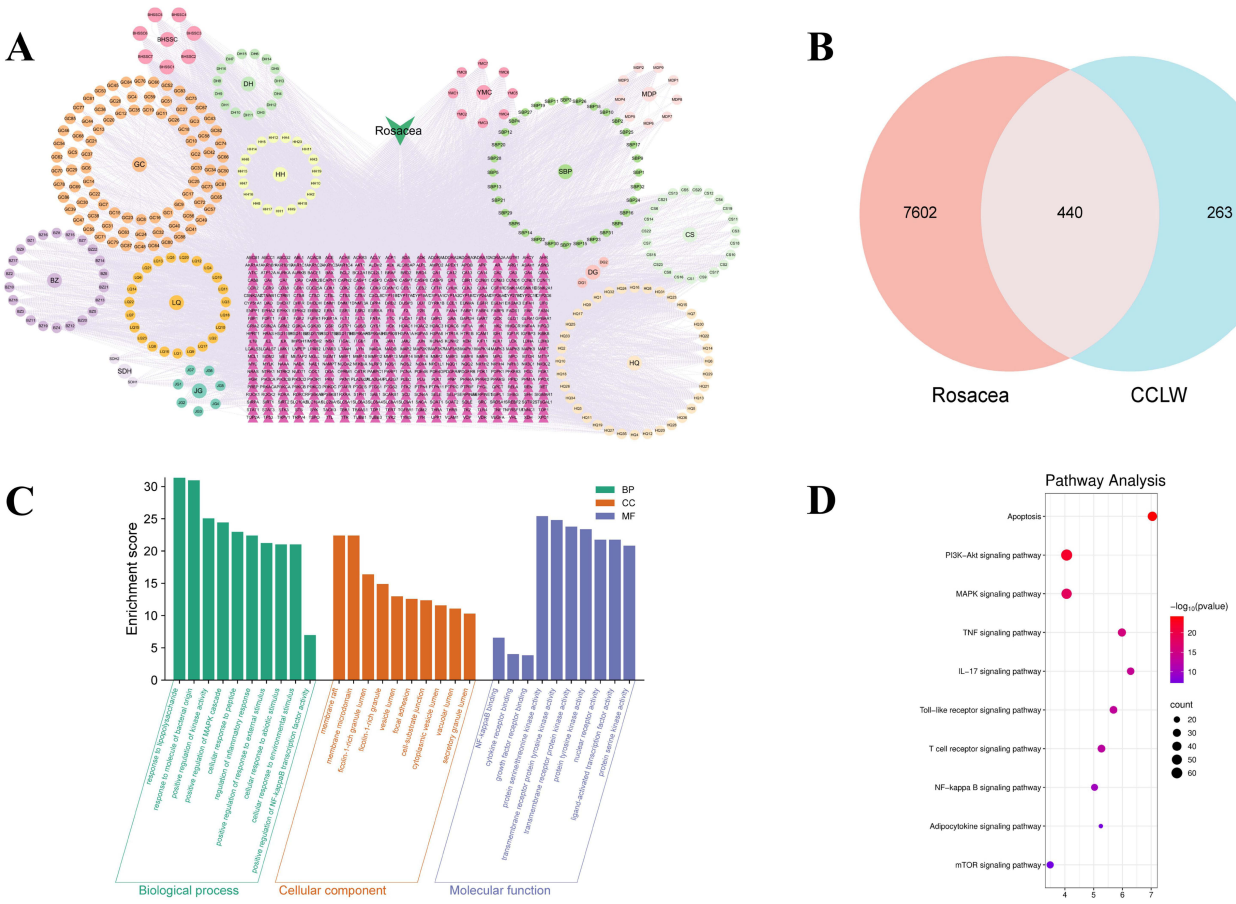

Figure 1 (**A**) Drug active ingredient-target network diagram for CCLP.The green triangles represent the disease, the red triangles represent all the targets of the disease, the center circles represent the CCLP drug components, and the circles around each drug component represent its compounds. (**B**) Drug-Disease Target Venn Diagram. (**C**) GO enrichment analysis graph. (**D**) Bubble map of KEGG enrichment analysis.

PPI Network Screening Targets and Enrichment Analysis

The protein-protein interaction network among the 17 consensus genes was analyzed using the STRING database (Figure 4A). Subsequently, a PPI network was constructed in Cytoscape 3.10.0, where targets were further screened based on median degree values, with increasing orange color intensity corresponding to higher degree values (Figure 4B). GO enrichment analysis revealed that CCLP treatment of rosacea was primarily associated with the following biological processes: collagen catabolic process, extracellular matrix disassembly, regulation of inflammatory response, collagen metabolic process, neuroinflammatory response, and positive regulation of leukocyte cell-cell adhesion (Figure 4C). Cellular component analysis identified tertiary granules, tertiary granule lumen, membrane rafts, membrane microdomains, ficolin-1-rich granule lumen, plasma membrane external side, cytoplasmic side of plasma membrane, ficolin-1-rich granules, cytoplasmic side of membrane, and mitochondrial outer membrane (Figure 4D). Molecular functions included serine-type endopeptidase activity, serine-type peptidase activity, serine hydrolase activity, metalloendopeptidase activity, metallopeptidase activity, collagen binding, endopeptidase activity, phospholipase binding, proteoglycan binding, and non-membrane spanning protein tyrosine kinase activity (Figure 4E). KEGG pathway enrichment analysis demonstrated significant involvement of the IL-17 signaling pathway, lipid and atherosclerosis, rheumatoid arthritis, NF-κB signaling pathway, and TNF signaling pathway among the top enriched pathways (Figure 4F and G).

https://doi.org/10.2147/CCID.S579507

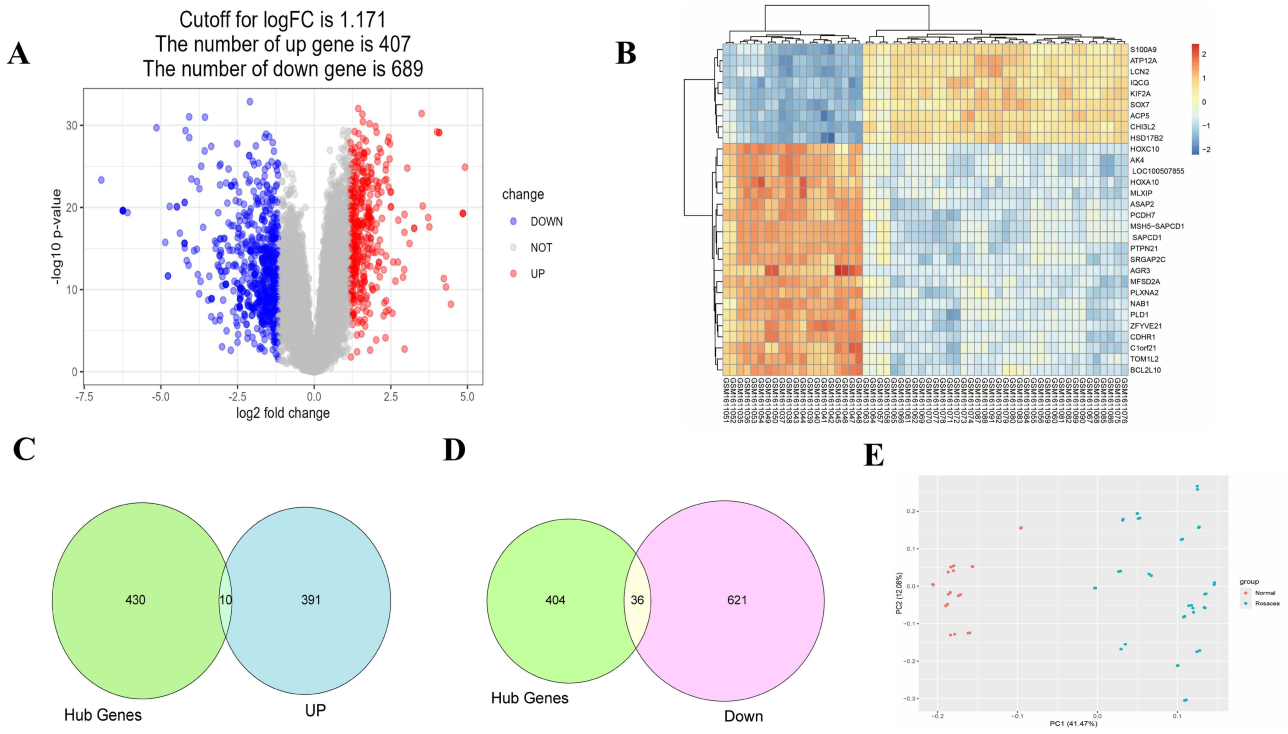

Figure 2 Targets and differentially expressed genes of CCLP active ingredients in Rosacea. (**A**) Volcano plot of differentially expressed genes from the GSE65914 dataset. Red and blue dots represent significantly upregulated and downregulated genes, respectively. (**B**) Heatmap of intersecting targets. (**C**) Intersection of CCLP with genes up-regulated by Rosacea targets. (**D**) Intersection of CCLP with genes down-regulated by Rosacea targets. (**E**) Principal component analysis plot of sample components.

R Screening for Core Targets

Three machine learning algorithms—LASSO, SVM, and RF—identified 11, 13, and 12 feature genes, respectively (Figure 5A–F). The intersection of these candidate targets yielded nine consensus genes: HK2, CTSS, AKR1B10, PTPRC, PTAFR, MMP9, IL1B, LCK, and ITK (Figure 5G).

ROC Diagnostic Model

To identify pivotal targets, we intersected the candidate genes derived from machine learning algorithms in R with those identified via PPI network analysis. This integration yielded seven core genes: CTSS, PTPRC, PTAFR, MMP9, IL1B, LCK, and ITK (Figures 6 and Figure 7A).

Analysis of the Relationship Between Core Genes and Immune Infiltration

Analysis of immune cell infiltration revealed distinct distribution patterns across samples (Figure 7B). Resting mast cells and resting dendritic cells constituted substantial proportions in multiple samples, while M0 macrophages, M1 macrophages, M2 macrophages, resting CD4 memory T cells, and plasma cells were also notably prevalent in specific samples. Comparative analysis between High and Low groups identified significant differences in five immune cell types: resting dendritic cells (****$p < 0.0001$), M0 macrophages (***$p < 0.001$), M1 macrophages (**$p < 0.01$), monocytes (*$p < 0.05$), and activated NK cells (**$p < 0.01$). These findings were consistent with the heatmap visualization of immune cell distribution (Figure 7C).Resting dendritic cells demonstrated higher infiltration levels in the Low group compared to the High group (Figure 7D). Correlation analysis between core genes and immune cells revealed distinct association patterns (Figure 7E). The seven core genes showed weak correlations with memory B cells and follicular helper T cells, while demonstrating no significant associations with naïve CD4+ T cells, gamma delta T cells, resting NK cells, activated mast cells, or eosinophils. Strong correlations were observed with plasma cells, CD8+ T cells, resting and activated CD4+ memory T cells, gamma delta T cells, activated NK cells, monocytes, M0/M1/M2 macrophages, and activated/resting

https://doi.org/10.2147/CCID.S579507

https://doi.org/10.2147/CCID.S579507

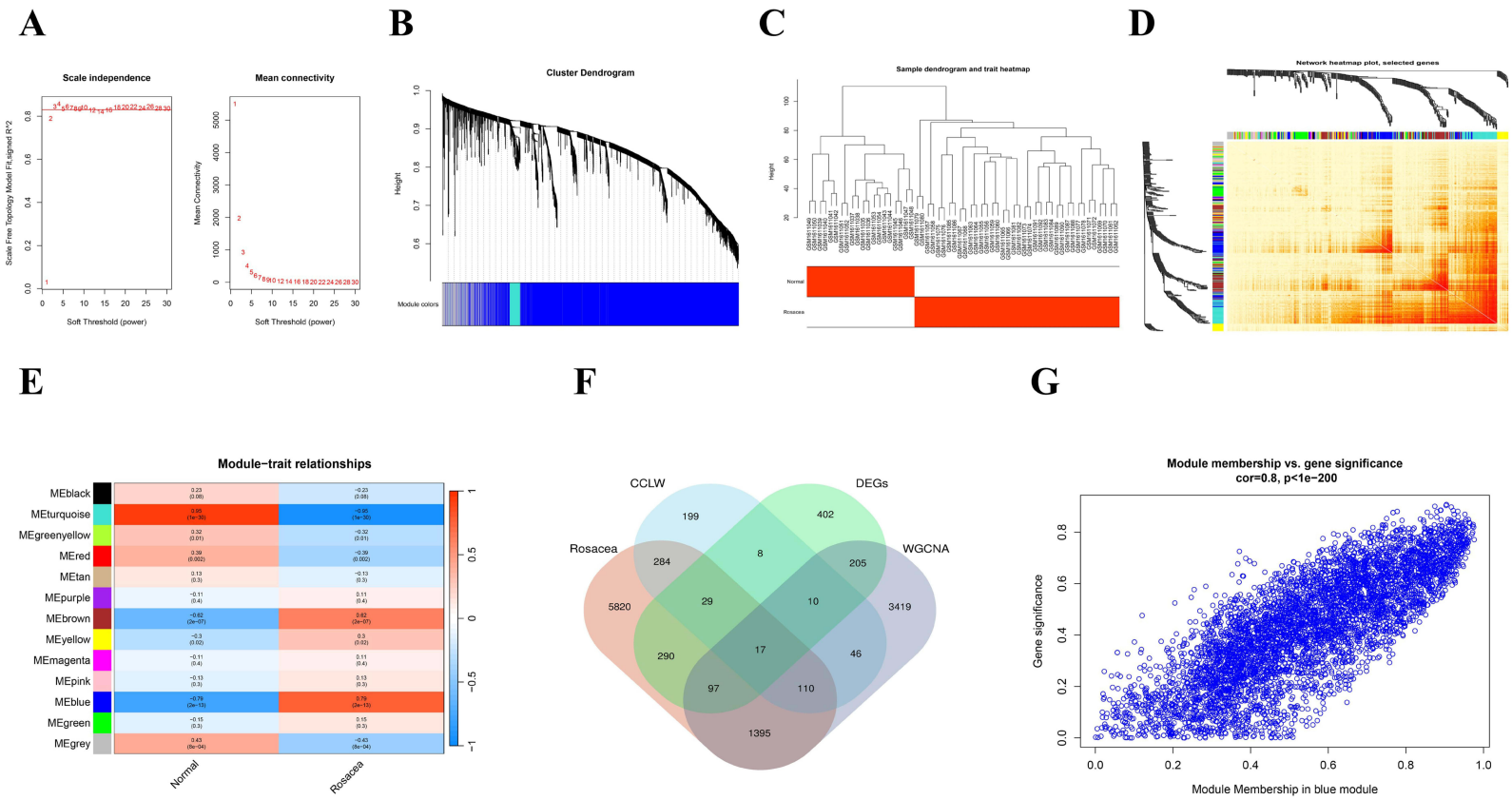

Figure 3 WGCNA analysis and core gene screening. (**A**) Soft-thresholding power selection; left: scale-free topology fit index; right: mean connectivity. (**B**) Gene cluster dendrogram with module color assignment. (**C**) Sample dendrogram and trait heatmap. (**D**) Topological overlap matrix (TOM) heatmap. (**E**) Module-trait correlations heatmap; red indicates positive correlation, blue indicates negative correlation. (**F**) Intersection of CCLP and Rosacea targets, red and blue represent Rosacea and CCLP, green and gray represent GEO and WGCNA datasets. (**G**) Scatterplot of gene module members versus gene significance.

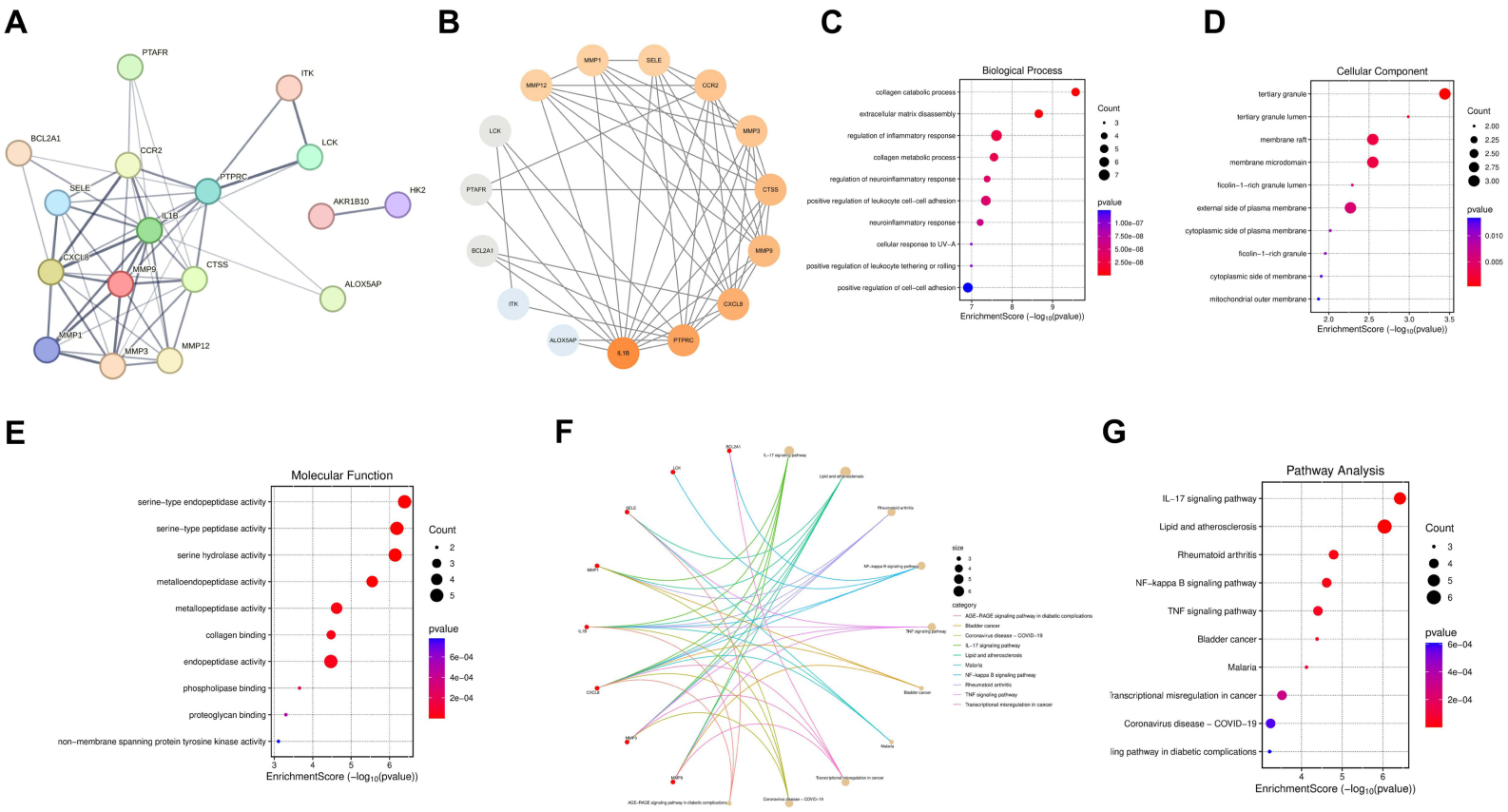

Figure 4 PPI network with enrichment analysis. (**A**) cross gene association graph. (**B**) core protein PPI network graph, larger circle and darker color indicate higher degree value. (**C**). GO enrichment analysis (Biological Process). (**D**) GO enrichment analysis (Cellular Component). (**E**) GO enrichment analysis (Molecular Function). (**F**) KEGG pathway enrichment analysis. (**G**) Top 10 significantly enriched KEGG pathways.

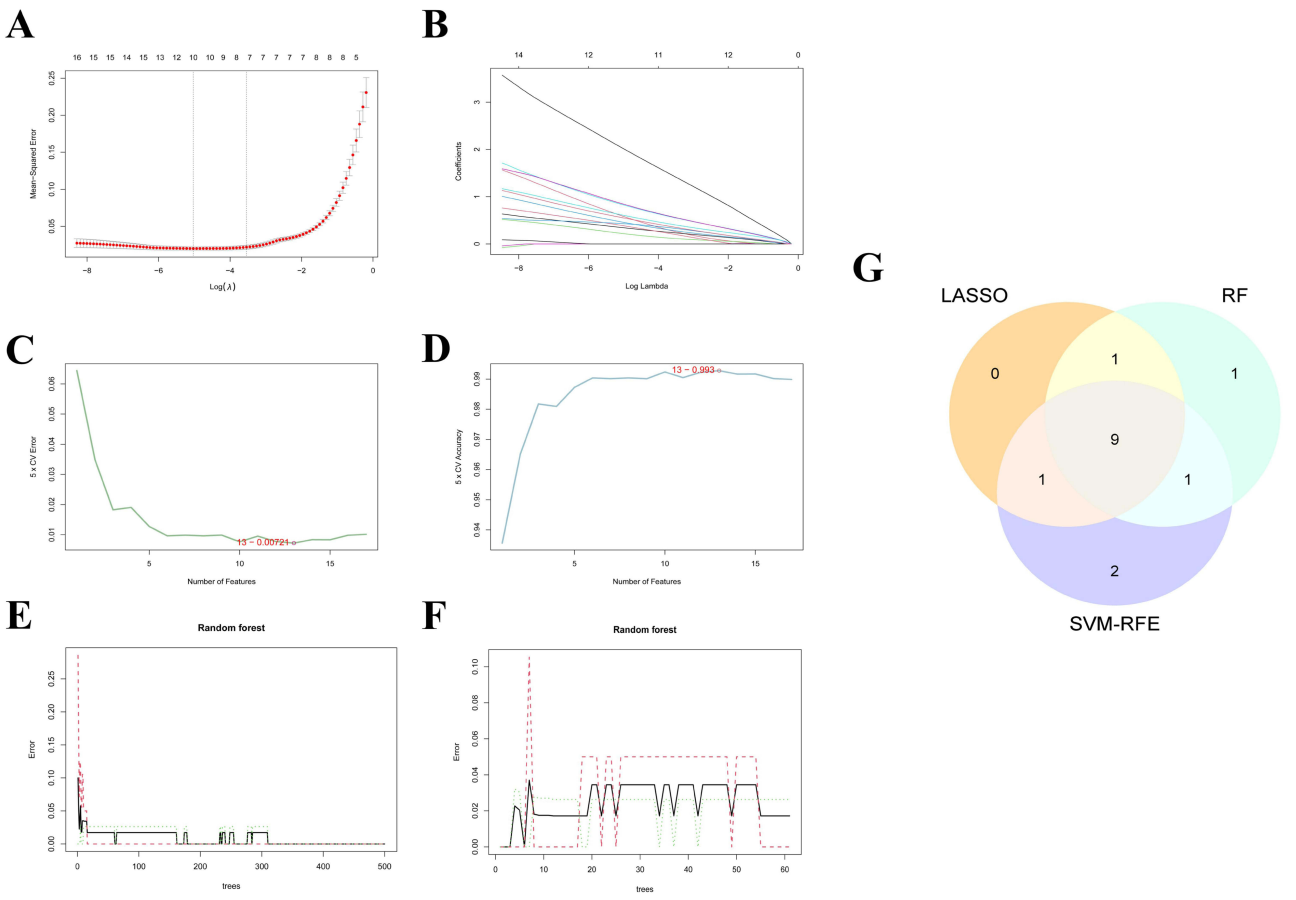

Figure 5 R Screening for Core Targets. (**A–F**) Predicted pivotal genes, (**A** and **B**) denote the data from LASSO. (**C** and **D**) denote the data from SVM, (**E** and **F**) denote the data from RF. (**G**) Intersection results of the three algorithms. Purple color represents SVM, yellow color represents LASSO, and green color represents RF.

dendritic cells. Among neutrophils, differential correlation patterns were noted: ITK, IL1B, PTAFR, and PTPRC showed weaker associations, whereas LCK, MMP9, and CTSS exhibited stronger correlations.

GSEA Analysis

Based on integrated bioinformatics analysis and supporting literature, IL-1β was identified as a core therapeutic target demonstrating high diagnostic value. Gene set enrichment analysis (GSEA) of IL-1β subsequently identified the NF-κB signaling pathway as the most significantly enriched pathway (Figure 8A and B). We therefore performed molecular docking studies to evaluate the binding between core CCLP components (eg, quercetin) and key targets (IL-1β, MMP9), followed by corresponding in vivo validation experiments.

Molecular Docking

To validate network pharmacology predictions, we performed molecular docking between IL1B and the top-ranked core targets. Binding energies below −5 kcal/mol indicate favorable ligand-target interaction, while values below −7 kcal/mol suggest strong binding affinity. Among the ten docking simulations, most exhibited binding energies lower than −6.3 kcal/mol, with a mean value of −6.91 kcal/mol, demonstrating robust binding between the compounds and core targets. These results support IL1B as a potential key target for CCLP in rosacea treatment. Interaction patterns were visualized using Discovery Studio 2019 (Figure 9). The optimal docking pose revealed that quercetin forms conventional hydrogen bonds with Tyr65, Lys65, and Ser5 of IL1B, along with π-alkyl interactions with Pro91 and Lys63 (Figure 9A).

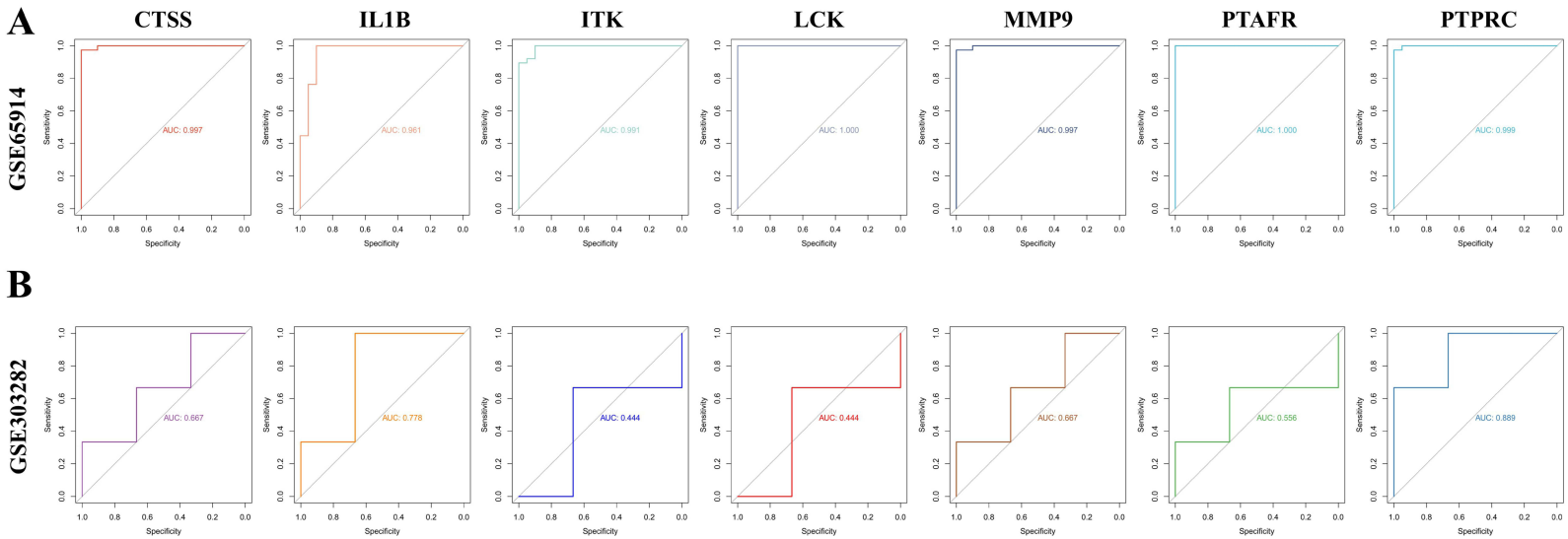

Figure 6 ROC diagnostic model. (**A**) ROC diagnostic model of 7 core genes in training set GSE65914 dataset. (**B**) ROC diagnostic model of 7 core genes in validation set GSE303282 dataset.

https://doi.org/10.2147/CCID.S579507

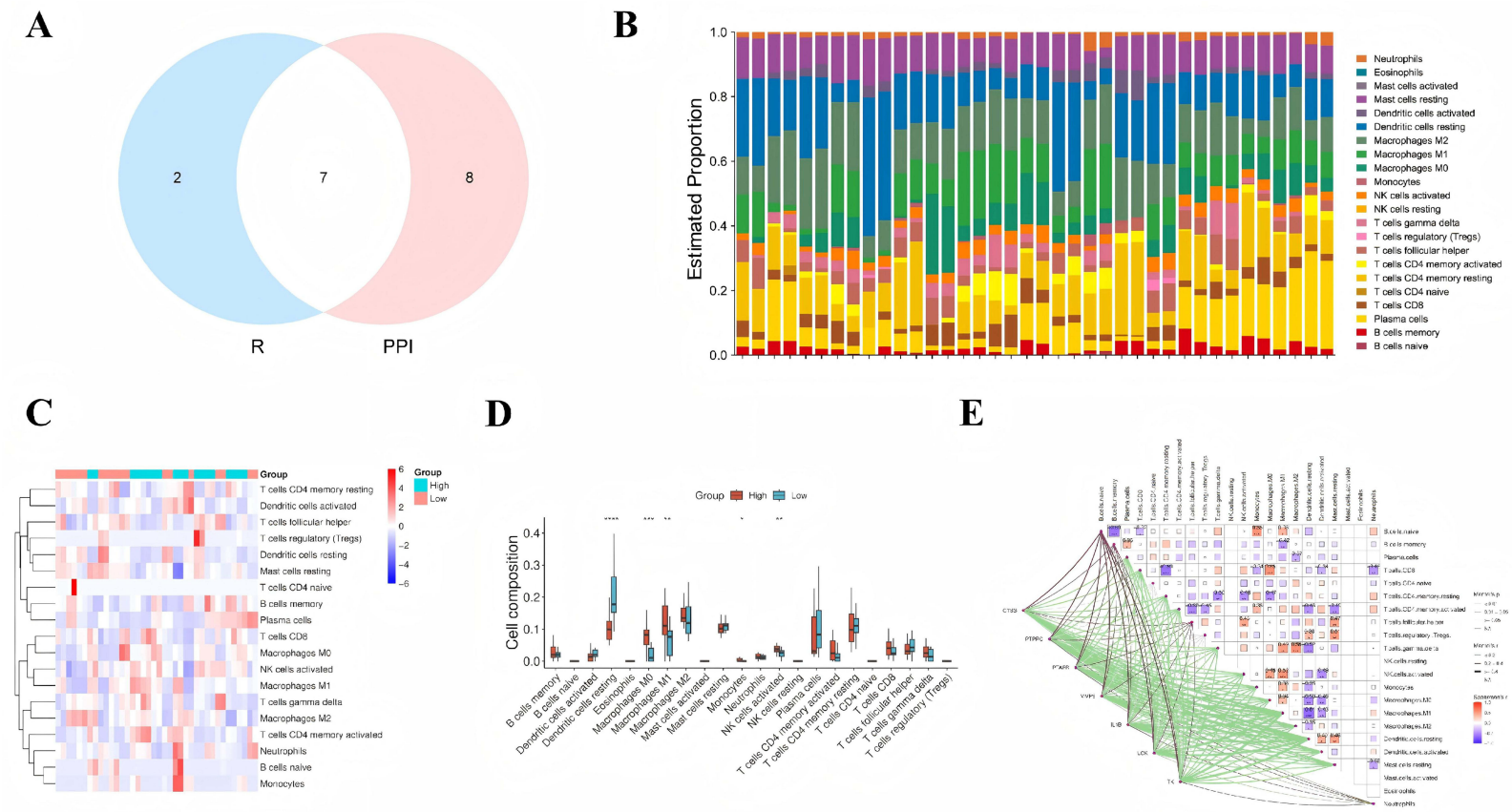

Figure 7 (**A**) Venn diagram of pivotal gene screening. Blue circles represent genes from the "R" analysis, pink circles represent genes from the PPI network analysis, and the overlapping region contains seven hub genes common to both analyses. (**B**) Stacked histogram showing the estimated proportions of the 22 immune cell subpopulations in the samples. Different colors represent different immune cell types and the y-axis indicates the proportions, with each column corresponding to a single sample. (**C**) Heatmap of the correlation between hub gene expression and immune cell infiltration, with the color scale (blue to red) representing the relative abundance or intensity of the correlation, the immune cell types listed on the right side, and the sample groups shown at the top. (**D**) Box line plot showing the cellular composition of different immune cell types in the High and Low groups proportions, asterisks indicate significant differences between groups (****:p < 0.0001,***:p < 0.001,**:p < 0.01,*:p < 0.05). (**E**) Network diagram showing the correlation between different immune cell types and specific genes. The squares on the right represent immune cell types and the dots on the left represent genes.

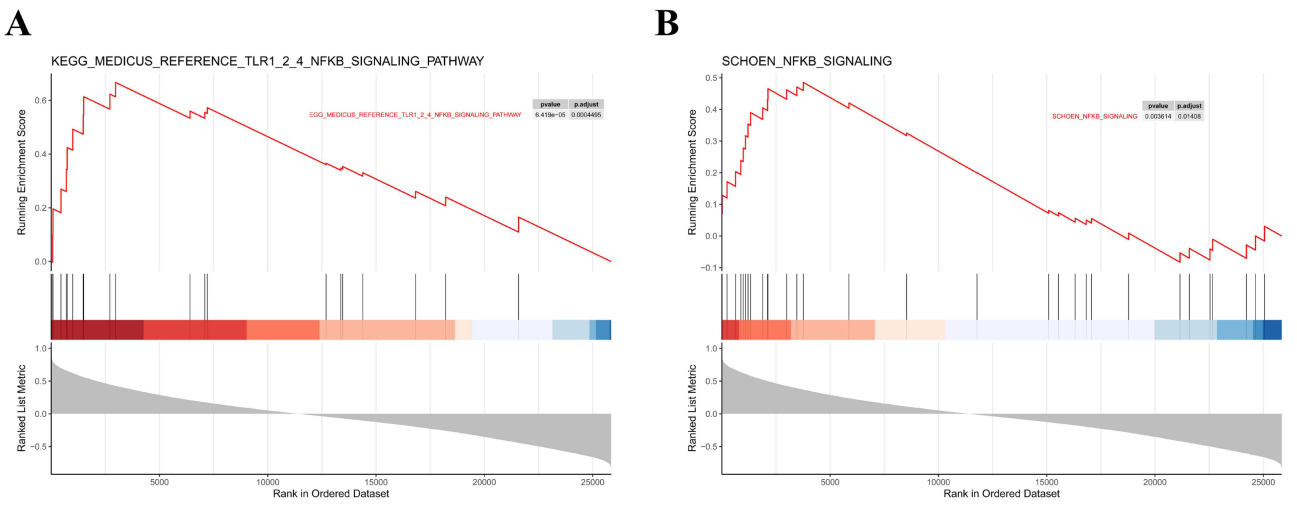

Figure 8 GSEA Enrichment Results.(**A**) KEGG_MEDICUS_REFERENCE_TLR1_2_4_NFKB_SIGNALING_PATHWAY.(**B**) SCHOEN_NFKB_SIGNALING.

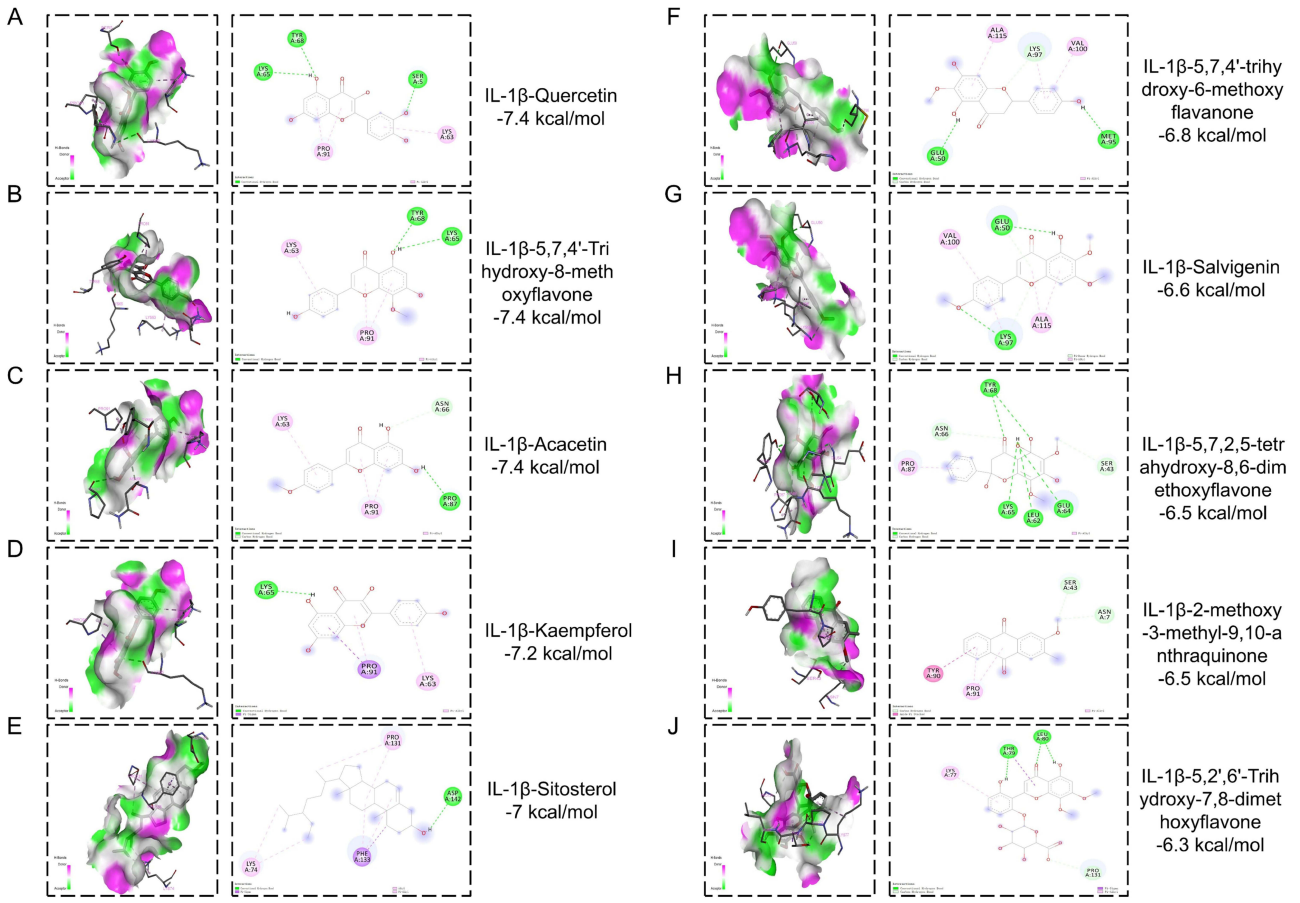

Figure 9 Molecular docking results showing the binding affinity of IL1B with each target protein. (Left: 3D local view; Right: 2D view). (**A**) IL1B-Quercetin. (**B**) IL-1β-5,7,4'-Trihydroxy-8-methoxyflavone. (**C**) IL-1β-Acacetin. (**D**) IL-1β-Kaempferol. (**E**) IL-1β-Sitosterol. (**F**) IL-1β-5,7,4'-trihydroxy-6-methoxyflavanone. (**G**) IL-1β-Salvigenin. (**H**) IL-1β-5,7,2,5-tetrahydroxy-8,6-dimethoxyflavone. (**I**) IL-1β-2-methoxy-3-methyl-9,10-anthraquinone. (**J**) IL-1β-5,2',6'-Trihydroxy-7,8-dimethoxyflavone.

https://doi.org/10.2147/CCID.S579507

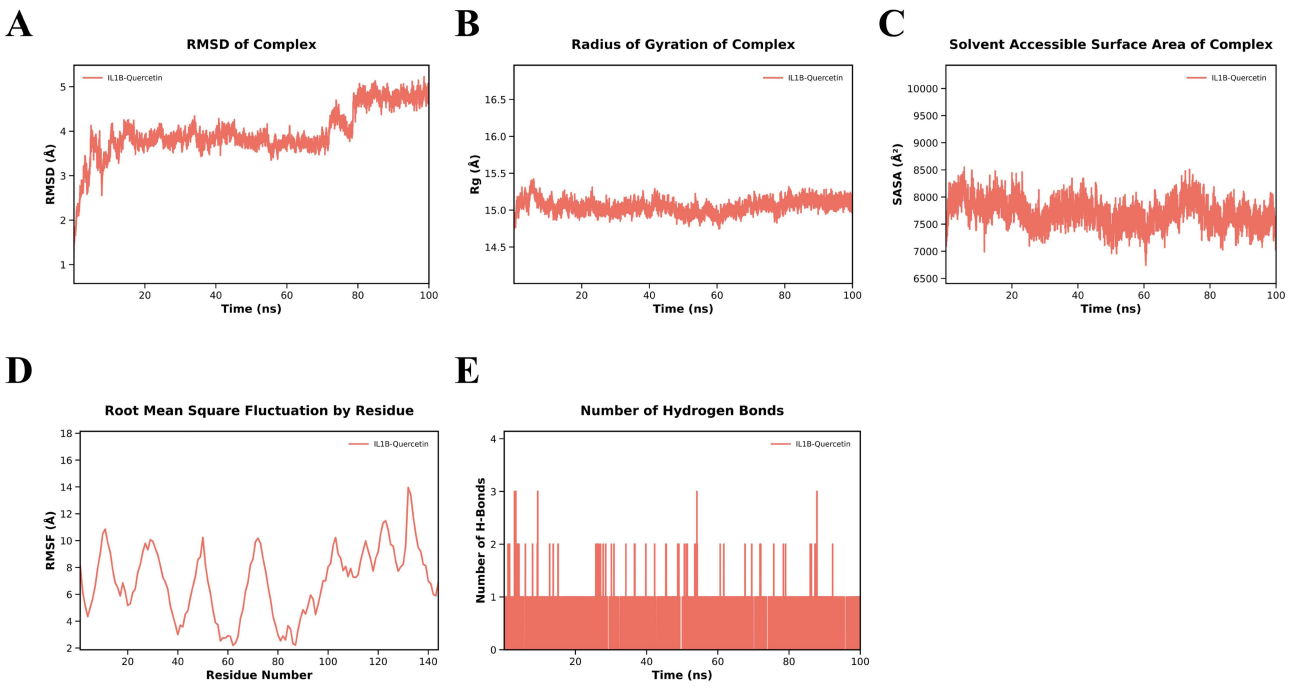

Figure 10 (**A**) RMSD curves for proteins and compounds. (**B**) Rg curves for protein-compound complexes. (**C**) SASA curves for protein-compound complexes. (**D**) RMSF analysis curves for proteins and compounds. (**E**) Hydrogen bond count curves for proteins and compounds.

Molecular Dynamics Simulation

To evaluate the structural stability and binding characteristics of the IL-1β-quercetin complex, we analyzed the 100 ns molecular dynamics simulation trajectory. The root mean square deviation (RMSD) of the complex remained stable within 2 Å throughout the simulation, indicating conformational equilibrium and high structural stability (Figure 10A). This was further supported by the radius of gyration (Rg) profile, which showed minimal fluctuation and preserved structural compactness, with only minor variations observed around 60 ns (Figure 10B).Solvent-accessible surface area (SASA) analysis revealed two notable peaks at approximately 20 ns and 60 ns, suggesting transient increases in solvent exposure that may influence complex solvation and conformational flexibility (Figure 10C). Root mean square fluctuation (RMSF) analysis demonstrated reduced flexibility in binding site residues, confirming the stabilizing effect of ligand binding on local protein structure (Figure 10D). Hydrogen bond analysis showed consistent formation of 1–2 bonds throughout the simulation, indicating maintained hydrophilic interactions (Figure 10E).The MM/GBSA binding free energy calculation yielded a ΔG_binding value of –162.18 ± 13.62 kJ/mol (Table 2), confirming strong binding affinity between quercetin and IL-1β, and validating the structural stability observed throughout the simulation.

Table 2 Free Energy Distribution of the Protein-IL1B-Quercetin Complex

Energy Type	Compound kJ/mol
Van der Waals energy	−162.1790±13.6160
Electrostatic energy	−26.3943±13.5808
Polar Solvation Contribution	83.7101±12.7499
Nonpolar solventization contribution	−17.7975±0.8335
ΔG_binding	−122.6607±14.8921

https://doi.org/10.2147/CCID.S579507

Experiment

Comparison of Erythema Severity Scores and Erythema Area

Six hours after the final administration, no significant changes were observed in the dorsal injection site of mice in the control group (Figure 11.Ai). In the model group, erythema with central edema or necrotic crusting formed at the local injection site (Figure 11.Aii). The erythema was markedly reduced in the doxycycline (DOX)-treated positive group (Figure 11.Aiii). Erythema was reduced to varying degrees in the low-, medium-, and high-dose CCLP groups after treatment (Figure 11.Aiv-vi).The erythema severity score and erythema area in the model group were significantly higher than those in the control group ($P < 0.0001$). Compared with the model group, both the severity score and erythema area were reduced in the CCLP medium-dose group ($P < 0.01$). The CCLP high-dose group exhibited a significant reduction in erythema area ($P < 0.001$) and erythema severity ($P < 0.0001$). The CCLP low-dose group showed no statistically significant difference ($P > 0.05$). (Figure 11B and C).

Comparative Pathological Lesions in H&E Staining

The skin structure of mice in the control group was intact, with uniform distribution of the epidermis, dermis, and subcutaneous tissue, and no inflammatory cell infiltration was observed. (Figure 12A) The model group exhibited marked skin tissue thickening, impaired skin barrier function, capillary proliferation, and extensive inflammatory cell infiltration. Compared with the model group, the CCLP high-dose group showed reduced skin thickening, significantly decreased inflammatory cell infiltration, and markedly improved capillary proliferation, with significant differences compared to the model group ($P < 0.01$). The positive control group exhibited significantly less inflammatory cell infiltration than the model group ($P<0.01$). Both the CCLP low- and medium-dose groups showed reduced inflammatory cell infiltration and improved skin thickening, but these differences were not statistically significant compared to the model group (all $P>0.05$). No statistically significant differences were observed between the CCLP low- and medium-dose groups ($P>0.05$). (Figure 12B).

Comparison of Mast Cell Infiltration

In the dermis of skin tissue from control -group mice, individual mast cells can be observed. (Figure 13A). These cells displayed characteristic pale blue cytoplasmic staining with a dispersed arrangement. Mast cell counts demonstrated

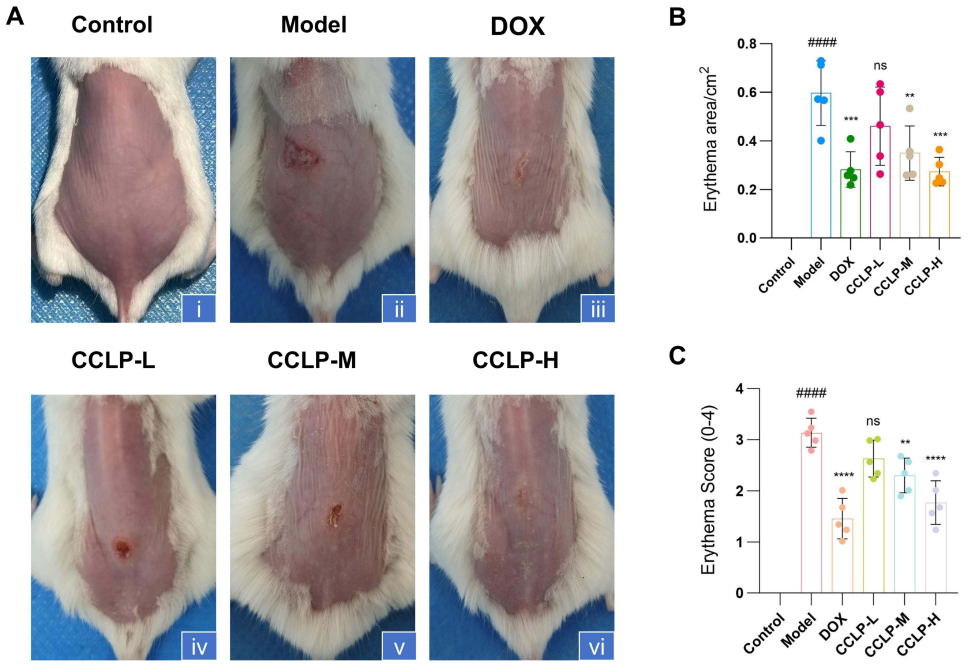

Figure 11 Macroscopic evaluation of skin lesions. (**A**). Representative photographs of dorsal skin lesions from six experimental groups 6 hours after the final administration. (**B**). Quantification of lesion area. (**C**). Erythema severity scores. Data are presented as mean ± SD. ####$P < 0.0001$ versus normal control group; **$P < 0.01$, ***$P < 0.001$, ****$P < 0.0001$ versus model control group; ns, not significant (one-way ANOVA with Tukey's post hoc test).

https://doi.org/10.2147/CCID.S579507

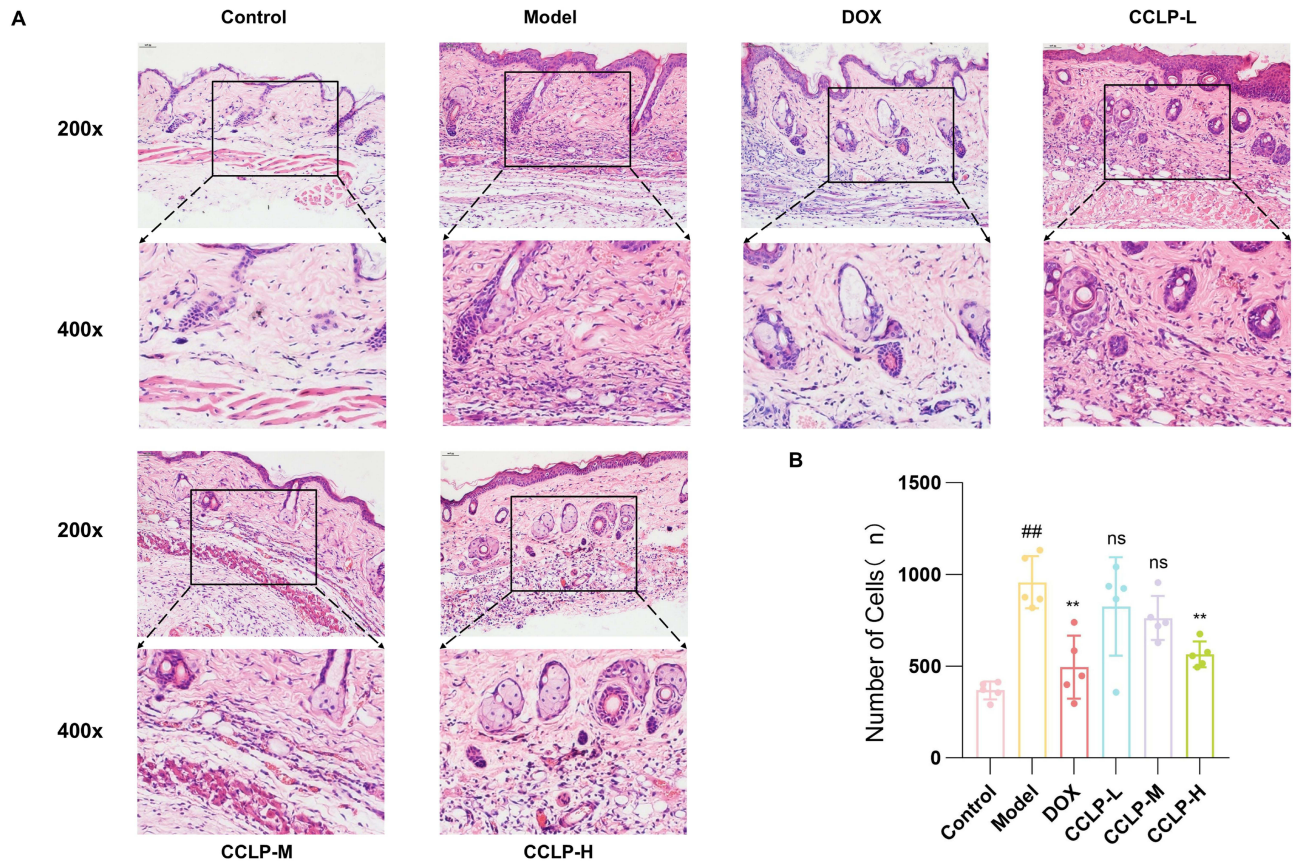

Figure 12 Histopathological evaluation of skin lesions by H&E staining. (**A**) Representative images of dorsal skin sections from different experimental groups. Scale bars: 100 μm (200×), 50 μm (400×). (**B**) Quantitative analysis of inflammatory cell infiltration at the injection site. Data are presented as mean ± SD; ##P < 0.01 versus normal control group; **P < 0.01 versus model control group; ns, not significant (one-way ANOVA with Tukey's post hoc test).

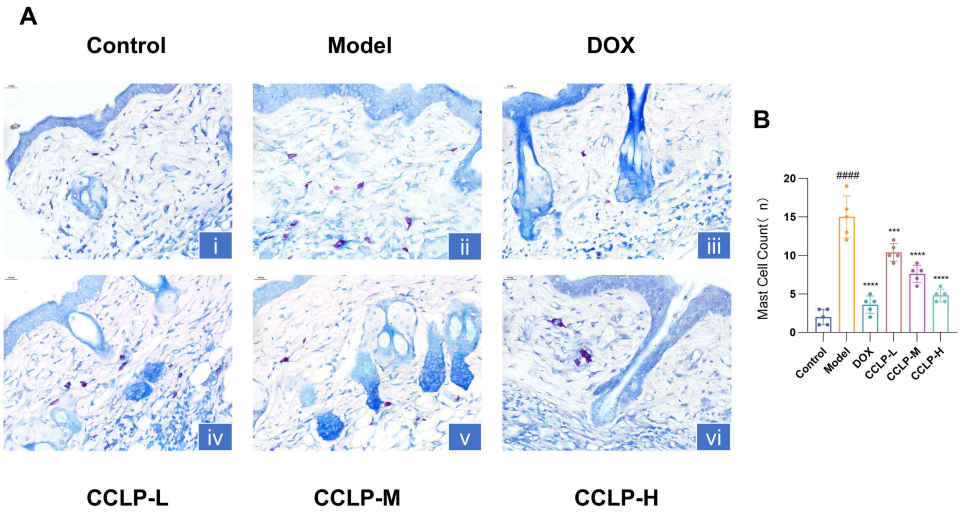

Figure 13 Toluidine blue staining. (**A**) Representative images of toluidine blue-stained skin sections from each group (scale bar: 50 μm). Mast cells are identified by metachromatic purple-blue granules. (**B**) Quantification of mast cell counts per field. Data are presented as mean ± SD. #####P < 0.0001 versus normal control group; ***P < 0.001, ****P < 0.0001 versus model control group (one-way ANOVA with Tukey's post hoc test).

https://doi.org/10.2147/CCID.S579507

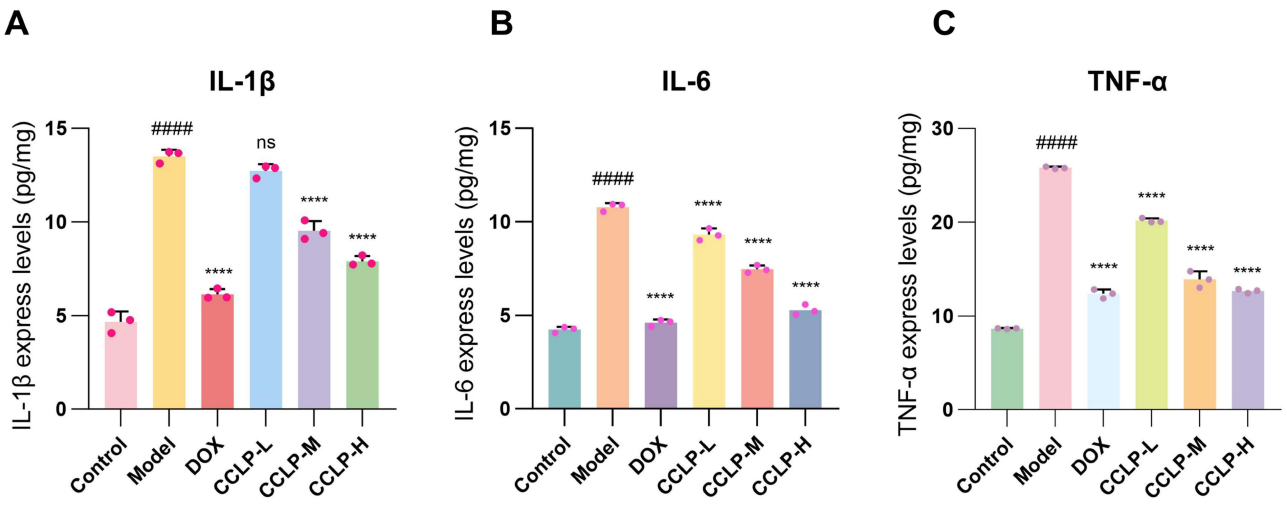

Figure 14 ELISA Test Data Chart. (**A**) IL-1β concentrations in skin tissues. (**B**) IL-6 levels. (**C**) TNF-α expression. Data are presented as mean ± SD. ####P < 0.0001 versus normal control group; ****P < 0.0001 versus model control group; ns, not significant (one-way ANOVA with Tukey's post hoc test).

a significant increase in the model group (15 ± 2.73 cells/field) compared to normal controls (2 ± 1 cells/field, P < 0.0001). CCLP treatment produced dose-dependent effects: low-dose (10.4 ± 1.14 cells/field) showed no significant reduction versus model group, while both mid-dose (7.6 ± 1.14 cells/field) and high-dose (4.8 ± 0.83 cells/field) groups exhibited substantial decreases (P < 0.0001). No statistical difference was observed between medium - and high-dose groups (Figure 13B).

Comparison of IL-1β, IL-6, and TNF-α Levels

Levels of IL-1β, IL-6, and TNF-α in skin lesions were significantly elevated in the model group compared to controls group (P < 0.0001). Both medium- and high-dose CCLP treatments substantially reduced all three cytokine levels versus the model group (P < 0.0001). The low-dose CCLP group showed significant decreases in IL-6 and TNF-α (P < 0.0001), but no significant reduction in IL-1β. No statistical differences were observed between CCLP medium- and high-dose groups for any cytokine (Figure 14).

Comparative Analysis of TLR2, KLK5, and MMP9 Protein Expression

Compared to normal controls, the model group demonstrated markedly increased protein expression of TLR2, KLK5, and MMP9 in skin lesion tissues (P < 0.0001; Figure 15A). High-dose CCLP treatment substantially suppressed TLR2, KLK5, and MMP9 protein expression compared to the model group (P < 0.0001). Medium-dose CCLP significantly reduced TLR2 and MMP9 levels (P < 0.0001) and decreased KLK5 expression (P < 0.001), while low-dose CCLP also suppressed MMP9 (P < 0.001), TLR2, and KLK5 (P < 0.01). No significant differences in TLR2 and MMP9 expression were observed between medium- and high-dose CCLP groups.(Figure 15B–D).

Discussion

Rosacea presents as a complex inflammatory dermatosis with multifaceted pathophysiology encompassing genetic susceptibility, innate immune activation, neurovascular dysregulation, and cutaneous microbiome alterations. The characteristic facial involvement frequently leads to substantial psychosocial comorbidity, with patients reporting characteristic symptoms including xerosis, burning sensations, and paresthesia, ultimately resulting in significantly impaired quality of life.[16] Current therapeutic strategies demonstrate notable limitations in achieving sustained remission and personalized management.This study integrates network pharmacology, WGCNA, machine learning algorithms, and immune infiltration analysis to systematically elucidate the potential mechanisms underlying the intervention of the CCLP in rosacea. Its efficacy and molecular basis were validated through molecular docking, molecular dynamics simulations, and animal models, providing new theoretical foundations and experimental support for the modernization of traditional Chinese medicine compounds and precision treatment of rosacea.

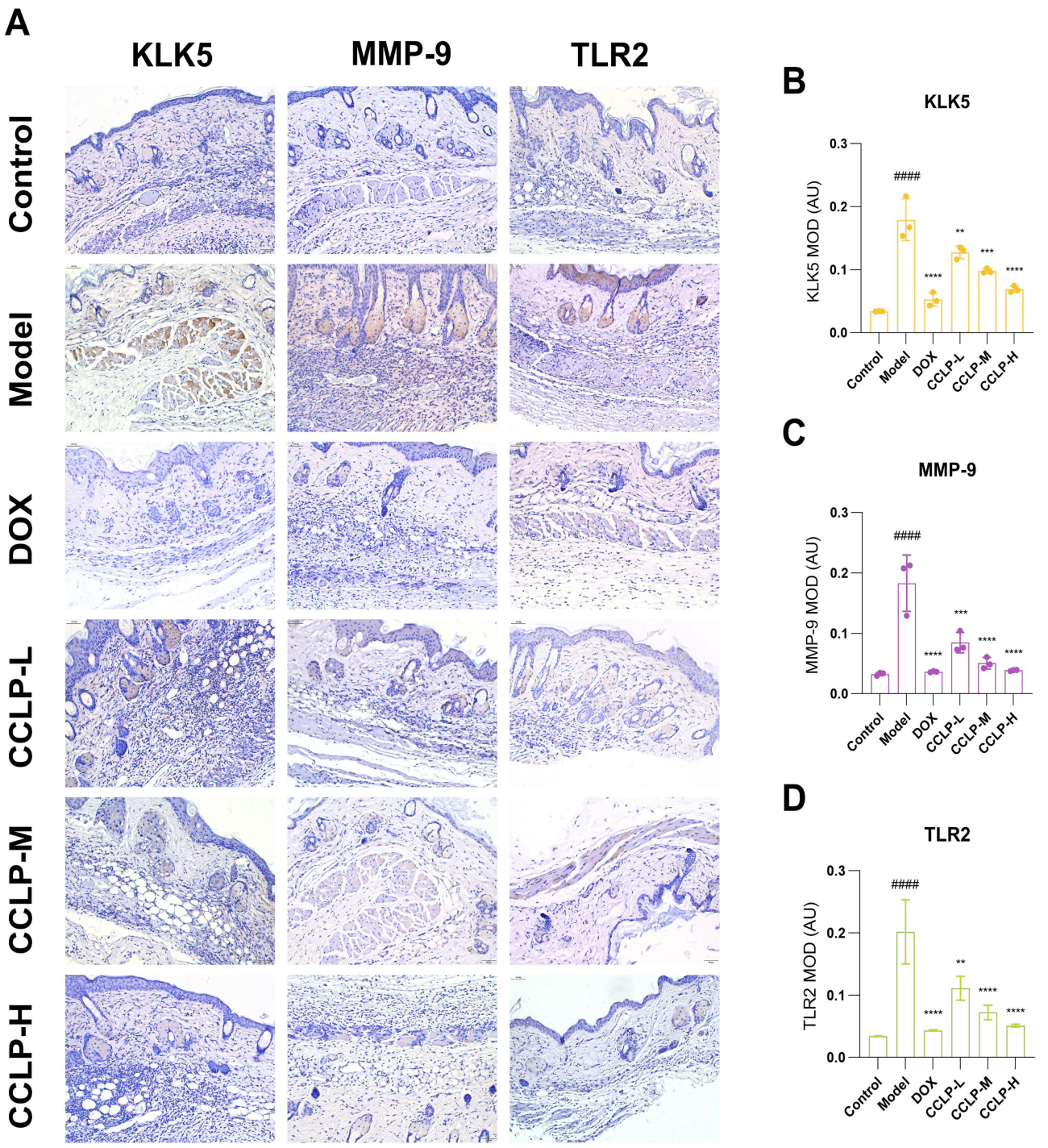

Figure 15 Immunohistochemical analysis of protein expression in skin lesions. (**A**) Representative immunohistochemical staining of TLR2, KLK5, and MMP9. (**B**) Quantitative analysis of KLK5. (**C**) Quantitative analysis of MMP9. (**D**) Quantitative analysis of TLR2 protein expression. Data are presented as mean ± SD. ####P < 0.0001 versus normal control group; **P < 0.01, ***P < 0.001, ****P < 0.0001 versus model control group (one-way ANOVA with Tukey's post hoc test).

Our analysis constructed a "component-target-disease"network that identified 703 potential CCLP targets against rosacea. These targets primarily regulate inflammatory responses, extracellular matrix remodeling, and immune cell activation. KEGG enrichment revealed IL-17, NF-κB, and TNF signaling pathways as key regulatory routes, suggesting CCLP's therapeutic mechanism involves suppression of Th17-mediated immunity and NF-κB-driven inflammation. WGCNA identified a disease-associated blue module ($r = 0.82$, $p < 0.001$) in the co-expression network. Integration

 https://doi.org/10.2147/CCID.S579507

with machine learning algorithms (LASSO, SVM-RFE, Random Forest) yielded seven core targets: CTSS, PTPRC, PTAFR, MMP9, IL1B, LCK, and ITK.Immune infiltration analysis demonstrated distinct IL1B expression patterns between High and Low groups. Resting dendritic cells showed significantly higher activity in the Low group ($p < 0.0001$), while monocytes, activated NK cells, and M0/M1 macrophages were elevated in the High group, suggesting positive correlation between these immune cell populations and IL1B-mediated inflammation.

To validate predictions from network pharmacology and bioinformatics analyses, we performed molecular docking between IL-1β—the core target identified through WGCNA and machine learning—and the top 10 active components of CCLP. Quercetin demonstrated strong binding affinity with IL-1β (binding energy = −7.4 kcal/mol). Molecular dynamics simulations further confirmed the structural stability of the quercetin-IL-1β complex, with RMSD fluctuations below 2 Å and minimal Rg variations. SASA analysis revealed increased solvent exposure at 20 ns and 60 ns, suggesting enhanced solvent interactions. The complex maintained structural integrity with low RMSF fluctuations in binding site residues and consistent hydrogen bonding (1–2 bonds).These findings align with established anti-inflammatory properties of quercetin.[17] As a abundant dietary flavonoid, quercetin modulates inflammation through multiple pathways, including suppression of TLR4-mediated cytokine production (IL-6, IL-1β) and inhibition of COX and lipoxygenase enzymes.[18] Previous studies by Yang et al demonstrated that quercetin reduces pro-inflammatory factors (IL-6, CXCL1, CXCL8) in keratinocytes from atopic dermatitis models, inhibits ERK/p38 phosphorylation, and suppresses histamine release and IgE production.[19] Additionally, quercetin ameliorates skin inflammation in psoriasiform and atopic dermatitis models through NF-κB pathway modulation while mitigating oxidative stress and promoting wound healing in human keratinocytes.[20]

The chronic inflammation in rosacea involves innate immune overactivation. IL-1β, an upstream regulator of the NF-κB pathway, shows elevated expression in murine rosacea lesions. Upon receptor binding, IL-1β triggers IκBα degradation via the MyD88-IKKβ cascade, facilitating p65/p50 nuclear translocation and subsequent transcription of pro-inflammatory mediators (TNF-α, IL-6, CXCL8) and LL-37. Our network pharmacology analysis identified the NF-κB pathway among the top 10 enriched pathways through KEGG analysis, supporting its relevance to CCLP's anti-inflammatory mechanism.The NF-κB pathway's involvement in dermatological pathologies is well-documented. Psoriatic lesions demonstrate elevated NF-κB activity,[21] while its inhibition ameliorates psoriasiform inflammation.[22] Similarly, atopic dermatitis involves HMGB1-TLR4-NF-κB signaling activation[23] and minocycline suppresses rosacea inflammation through TLR4-NF-κB pathway inhibition.[24] Furthermore, NF-κB activation promotes NLRP3 inflammasome formation and IL-1β production, contributing to keratinocyte inflammation under oxidative stress and potentially initiating melanocyte damage in vitiligo.[25] Although NF-κB activation patterns vary across dermatoses, this pathway consistently emerges as a central regulator of skin inflammation and disease progression. Targeting NF-κB signaling may therefore represent a promising therapeutic strategy for multiple inflammatory skin conditions, including rosacea. However, the hyperactivation of the NF-κB pathway is not only derived from the direct recognition of pathogens by keratinocytes, but is also precisely regulated by the infiltration of dermal immune cells (such as mast cells).

Mast cells infiltration has gained recognition as a diagnostically significant feature in dermatopathology, serving as a key diagnostic criterion for cutaneous mastocytosis.[26] In rosacea, mast cells contribute to inflammation through release of inflammatory mediators (histamine, leukotrienes, prostaglandins) and cytokines (TNF-α, IL-1β).[27–29] Previous studies by Zhou et al documented increased mast cell numbers and activation states in psoriatic lesions, accompanied by elevated proinflammatory cytokines including IL-1β, IL-6, and TNF-α.[30,31] Mast cell density and their production of inflammatory cytokines (IL-4, IL-13) correlate with disease severity in atopic dermatitis,[32] while in vitiligo, mast cell infiltration and degranulation accelerate disease progression through inflammatory mediator release.In rosacea pathogenesis, TLR2, KLK5, and MMP9 form an interconnected network: TLR2 activation stimulates KLK5 production in keratinocytes, while MMP9 facilitates KLK5 activation and processes cathelicidin into LL-37. LL-37 subsequently induces proinflammatory cytokine production (IL-1β, IL-6, TNF-α) via JAK/STAT, NF-κB, and NLRP3 signaling pathways, thereby sustaining inflammatory responses and promoting angiogenesis.[33,34] Furthermore, LL-37 amplifies inflammation through autocrine binding to TLR2 and subsequent mTORC1 pathway activation, establishing a proinflammatory feedback loop.[35]

Based on our findings, we validated the therapeutic efficacy of CCLP in a rosacea animal model. Medium- and high-dose CCLP treatment reduced erythema area by 40–60% and severity scores by 50–70%, demonstrating comparable efficacy to doxycycline positive control. Histopathological examination revealed significant improvements in epidermal

thickness, capillary proliferation, and inflammatory cell infiltration. Mast cell counts in rosacea-affected skin decreased from 15 to 4.8 cells/field following CCLP treatment. ELISA results confirmed that medium and high CCLP doses significantly reduced IL-1β, IL-6, and TNF-α levels. Immunohistochemical analysis further demonstrated substantial downregulation of TLR2, KLK5, and MMP9 protein expression in CCLP-treated groups. These results indicate that CCLP effectively ameliorates rosacea symptoms through potent anti-inflammatory mechanisms, providing compelling experimental evidence for its therapeutic application in rosacea management.

In summary, our integrated approach identified IL-1β as the core therapeutic target. Initially, network pharmacology predicted that CCLP might exert its therapeutic effects by suppressing Th17-mediated immune responses and NF-κB-driven inflammation. Subsequently, bioinformatic analysis cross-validated the phenotype-associated targets derived from WGCNA with those identified by three machine learning algorithms—LASSO, SVM-RFE, and Random Forest—which collectively pinpointed IL-1β as the central target. Molecular docking and molecular dynamics simulations provided structural validation, demonstrating strong and stable binding between IL-1β and the top-ranking bioactive compounds within the CCLP compound-target network. Finally, in vivo animal experiments confirmed the functional relevance, as CCLP treatment significantly modulated IL-1β expression. Therefore, converging evidence from these complementary investigative tiers establishes IL-1β, a key upstream regulator of the NF-κB pathway, as the pivotal node mediating CCLP's therapeutic action against rosacea.

While this study advances our understanding of CCLP's therapeutic mechanisms in rosacea, several limitations warrant consideration. First, the animal model employed primarily replicates acute erythematous rosacea and does not fully replicate the pathological features of other rosacea subtypes. Second, the absence of clinical sample validation necessitates further investigation to confirm core target expression and function in human lesions. Although bioinformatic analyses implicated NF-κB signaling in CCLP's mechanism, this requires direct validation through molecular biology techniques such as Western blotting and RT-qPCR.Future research should incorporate multi-omics approaches including proteomics and metabolomics to comprehensively elucidate CCLP's molecular mechanisms. Additionally, well-designed multicenter, randomized, double-blind clinical trials will be essential to systematically evaluate CCLP's efficacy and safety across different rosacea subtypes.

Conclusions

This integrated study demonstrates, through network pharmacology, bioinformatic analysis, molecular docking, molecular dynamics simulations, and animal experimental validation, that CCLP exerts therapeutic effects against rosacea primarily via modulation of the TLR2/NF-κB signaling pathway. In LL-37-induced murine models, CCLP treatment significantly alleviated disease progression, suppressed key inflammatory mediators (IL-1β, TNF-α, IL-6), downregulated critical proteins (TLR2, KLK5, MMP9), and reduced mast cell infiltration. These findings establish CCLP as a promising therapeutic candidate for rosacea and provide a solid mechanistic foundation for its clinical development. Translating this knowledge will require subsequent correlation studies in human patient samples to confirm target engagement and therapeutic relevance.

Abbreviations

CCLP, Cuochuangling pills; WGCNA, weighted gene co-expression network analysis; ETR, erythematotelangiectatic; PPR, papulopustular; PHR, phymatous ; OR, ocular rosacea ; GSEA, Gene Set Enrichment Analysis; MD, molecular dynamics; ELISA, enzyme-linked immunosorbent assay; H&E, Hematoxylin-eosin staining; GO, Gene Ontology; KEGG, Genes and Genomes.

Data Sharing Statement

The dataset(s) supporting the conclusions of this articles (are) available in the GEO (https://www.ncbi.nlm.nih.gov/geo/), Genecard (https://www.genecards.org/), OMIM (https://omim.org/) and CTD (https://ctdbase.org/).

Ethics Approval and Consent to Participate

According to Article 32 of the Measures for Ethical Review of Life Science and Medical Research Involving Human Subjects (promulgated by the National Health Commission of the People's Republic of China, effective February 18,

2023), research involving the use of human information data or biological specimens under the following circumstances may be exempt from ethical review, provided that it causes no harm to human subjects, does not involve sensitive personal information, and does not entail commercial interests:

(1) Research conducted using legally obtained publicly available data, or data generated through observation without interfering with public behavior;

(2) Research conducted using anonymized information data;

In accordance with the above national legislation, this study is exempt from ethical review. No additional approval from an institutional review board was required for the bioinformatics component.

All animal experimental procedures were conducted in strict accordance with the 3Rs principles (Replacement, Reduction, and Refinement) and were approved by the Animal Ethics Committee of Shaanxi Provincial Hospital of Chinese Medicine (Approval No.: (2025) 15).

Consent to Publish

All authors gave their consent for publication.

Author Contributions

All authors made a significant contribution to the work reported, whether that is in the conception, study design, execution, acquisition of data, analysis and interpretation, or in all these areas; took part in drafting, revising or critically reviewing the article; gave final approval of the version to be published; have agreed on the journal to which the article has been submitted; and agree to be accountable for all aspects of the work.

Funding

This study was jointly supported by the Shaanxi Provincial Key Research and Development Program: "Assessing the Clinical Efficacy of Cuochuangling Pills (CCLP) in Rosacea with Blood-Heat Pattern and Exploration of Underlying Immune Mechanisms" (Grant No. S2025-YF-YBSF-0246) and the National Natural Science Foundation of China Project: "The Mechanism of Yin Xie Ping Tablets in Ameliorating Psoriasis with Damp-Heat Syndrome via PPARγ-Mediated Reprogramming of Glucose Metabolism in Keratinocytes" (Grant No. 82174386).

Disclosure

The authors declare that no competing or conflicting interests exist for this work.

References

1. van Zuuren EJ, Arents BWM, van der Linden MMD, Vermeulen S, Fedorowicz Z, Rosacea TJ. New concepts in classification and treatment. *Am J Clin Dermatol*. 2021;22(4):457–465. doi:10.1007/s40257-021-00595-7
2. Wang Z, Zhang Z. Advances in genetic polymorphism research in rosacea: mechanisms and clinical implications. *Clin Cosmet Investig Dermatol*. 2025;18:1423–1429. doi:10.2147/ccid.S524611
3. Schaller M, Almeida LMC, Bewley A, et al. Recommendations for rosacea diagnosis, classification and management: update from the global ROSacea COnsensus 2019 panel. *Br J Dermatol*. 2020;182(5):1269–1276. doi:10.1111/bjd.18420
4. Gether L, Overgaard LK, Egeberg A, Thyssen JP. Incidence and prevalence of rosacea: a systematic review and meta-analysis. *Br J Dermatol*. 2018;179(2):282–289. doi:10.1111/bjd.16481
5. Alexis AF, Callender VD, Baldwin HE, Desai SR, Rendon MI, Taylor SC. Global epidemiology and clinical spectrum of rosacea, highlighting skin of color: review and clinical practice experience. *J Am Acad Dermatol*. 2019;80(6):1722–1729.e7. doi:10.1016/j.jaad.2018.08.049
6. Rodrigues-Braz D, Zhao M, Yesilirmak N, Aractingi S, Behar-Cohen F, Bourges JL. Cutaneous and ocular rosacea: common and specific physiopathogenic mechanisms and study models. *Mol Vis*. 2021;27:323–353.
7. Okwundu N, Cline A, Feldman SR. Difference in vasoconstrictors: oxymetazoline vs. brimonidine. *J Dermatolog Treat*. 2021;32(2):137–143. doi:10.1080/09546634.2019.1639606
8. Searle T, Ali FR, Al-Niaimi F. The versatility of azelaic acid in dermatology. *J Dermatolog Treat*. 2022;33(2):722–732. doi:10.1080/09546634.2020.1800579
9. Andrade FMX, Picosse FR, Cunha LPD, et al. Ocular surface changes in the treatment of rosacea: comparison between low-dose oral isotretinoin and doxycycline. *Arq Bras Oftalmol*. 2020;83(2):109–112. doi:10.5935/0004-2749.20200016
10. Zhang Y, Jiang S, Lu Y, et al. A decade retrospective study of light/laser devices in treating nasal rosacea. *J Dermatolog Treat*. 2020;31(1):84–90. doi:10.1080/09546634.2019.1580669

11. Li J, Wei Y, Li X, et al. Herbal formula Xian-Fang-Huo-Ming-Yin regulates differentiation of lymphocytes and production of pro-inflammatory cytokines in collagen-induced arthritis mice. *BMC Complement Altern Med*. 2017;17(1):12. doi:10.1186/s12906-016-1526-x
12. Zhang R, Ma C, Wei Y, et al. Isolation, purification, structural characteristics, pharmacological activities, and combined action of Hedyotis diffusa polysaccharides: a review. *Int J Biol Macromol*. 2021;183:119–131. doi:10.1016/j.ijbiomac.2021.04.139
13. Lam P, Cheung F, Tan HY, Wang N, Yuen MF, Feng Y. Hepatoprotective effects of chinese medicinal herbs: a focus on anti-inflammatory and anti-oxidative activities. *Int J Mol Sci*. 2016;17(4):465. doi:10.3390/ijms17040465
14. Kee JY, Inujima A, Andoh T, et al. Inhibitory effect of Moutan Cortex aqueous fraction on mast cell-mediated allergic inflammation. *J Nat Med*. 2015;69(2):209–217. doi:10.1007/s11418-014-0880-6
15. Xu C, Shi F, Ding W, Fang C, Fang C. Development and validation of a machine learning model for cardiovascular disease risk prediction in type 2 diabetes patients. *Sci Rep*. 2025;15(1):32818. doi:10.1038/s41598-025-18443-7
16. Bewley A, Fowler J, Schöfer H, Kerrouche N, Rives V. Erythema of rosacea impairs health-related quality of life: results of a meta-analysis. *Dermatol Ther*. 2016;6(2):237–247. doi:10.1007/s13555-016-0106-9
17. Al-Khayri JM, Sahana GR, Nagella P, Joseph BV, Alessa FM, Al-Mssallem MQ. Flavonoids as potential anti-inflammatory molecules: a review. *Molecules*. 2022;27(9):2901. doi:10.3390/molecules27092901
18. Aggarwal D, Chaudhary M, Mandotra SK, et al. Anti-inflammatory potential of quercetin: from chemistry and mechanistic insight to nanoformulations. *Curr Res Pharmacol Drug Discov*. 2025;8:100217. doi:10.1016/j.crphar.2025.100217
19. Yang SC, Chang ZY, Hsiao CY, et al. Topical Anti-inflammatory effects of quercetin glycosides on atopic dermatitis-like lesions: influence of the glycone type on efficacy and skin absorption. *Inflammation*. 2025;48(5):2856–2873. doi:10.1007/s10753-025-02236-1
20. Liu HM, Cheng MY, Xun MH, et al. Possible mechanisms of oxidative stress-induced skin cellular senescence, inflammation, and cancer and the therapeutic potential of plant polyphenols. *Int J Mol Sci*. 2023;24(4):3755. doi:10.3390/ijms24043755
21. Al-Shobaili HA, Farhan J, Zafar U, Rasheed Z. Functional role of human interleukin-32 and nuclear transcription factor-kB in patients with psoriasis and psoriatic arthritis. *Int J Health Sci*. 2018;12(3):29–34.
22. Meng Q, Bai M, Guo M, et al. Inhibition of serum- and glucocorticoid-regulated protein kinase-1 aggravates imiquimod-induced psoriatic dermatitis and enhances proinflammatory cytokine expression through the NF-kB pathway. *J Invest Dermatol*. 2023;143(6):954–964. doi:10.1016/j.jid.2022.12.013
23. Vafaeian A, Rajabi F, Rezaei N. Toll-like receptors in atopic dermatitis: pathogenesis and therapeutic implications. *Heliyon*. 2025;11(3):e42226. doi:10.1016/j.heliyon.2025.e42226
24. Hua P, Tu Y, Yang Z, et al. Minocycline inhibits rosacea-like inflammation through the TLR4-mediated NF-κB signaling pathway in vivo and in vitro. *PLoS One*. 2025;20(5):e0323598. doi:10.1371/journal.pone.0323598
25. Faraj S, Kemp EH, Gawkrodger DJ. Patho-immunological mechanisms of vitiligo: the role of the innate and adaptive immunities and environmental stress factors. *Clin Exp Immunol*. 2022;207(1):27–43. doi:10.1093/cei/uxab002
26. Urbina F, Benavides A. Telangiectatic mastocytosis: if it is not mastocytosis, what is it? Comment on brockow et al. challenges in the diagnosis of cutaneous mastocytosis. diagnostics 2024, 14, 161. *Diagnostics*. 2025;15(11):1370. doi:10.3390/diagnostics15111370
27. Fisher GW, Travers JB, Rohan CA. Rosacea pathogenesis and therapeutics: current treatments and a look at future targets. *Front Med*. 2023;10:1292722. doi:10.3389/fmed.2023.1292722
28. Dahlan NH, Sitohang IBS, Indriatmi W, Wibowo H, Enggy LE. Correlation between reduced IL-1β levels in acne lesions and the decrease in acne inflammatory lesions following topical vitamin D administration: a double-blind randomized controlled trial. *Clin Cosmet Investig Dermatol*. 2024;17:2183–2195. doi:10.2147/ccid.S475068
29. Wang X, Shi H, Li X, Feng Y. Macrophages in rosacea: pathogenesis and therapeutic potential. *Front Immunol*. 2025;16:1595493. doi:10.3389/fimmu.2025.1595493
30. Zhou XY, Chen K, Zhang JA. Mast cells as important regulators in the development of psoriasis. *Front Immunol*. 2022;13:1022986. doi:10.3389/fimmu.2022.1022986
31. Song Q, Xu P, Xiao Q, Zhang C, Mao Y. Crosstalk between white adipose tissue and skin: unraveling its role in psoriasis pathogenesis (Review). *Mol Med Rep*. 2025;31(6):1–9. doi:10.3892/mmr.2025.13534
32. Chen Y, Griffiths CEM, Bulfone-Paus S. Exploring mast cell-CD8 T cell interactions in inflammatory skin diseases. *Int J Mol Sci*. 2023;24(2). doi:10.3390/ijms24021564
33. Yang F, Wang L, Song D, et al. Signaling pathways and targeted therapy for rosacea. *Front Immunol*. 2024;15:1367994. doi:10.3389/fimmu.2024.1367994
34. Woo YR, Lim JH, Cho DH, Park HJ. Rosacea: molecular mechanisms and management of a chronic cutaneous inflammatory condition. *Int J Mol Sci*. 2016;17(9). doi:10.3390/ijms17091562
35. Deng Z, Chen M, Liu Y, et al. A positive feedback loop between mTORC1 and cathelicidin promotes skin inflammation in rosacea. *EMBO Mol Med*. 2021;13(5):e13560. doi:10.15252/emmm.202013560